Rotor Structural Loads Analysis Using Coupled Computational Fluid Dynamics/Computational Structural Dynamics

Hyeonsoo Yeo **Mark Potsdam**
US Army Aviation Development Directorate – AFDD
Aviation & Missile Research, Development & Engineering Center
Research, Development, and Engineering Command
Ames Research Center, Moffett Field, California

ABSTRACT

Coupled CFD/CSD (RCAS/Helios and CAMRAD II/Helios) analyses are performed and the calculated rotor structural loads are compared with the flight test data obtained from the NASA/Army UH-60A Airloads Program. Three challenging level flight conditions are investigated: 1) high speed with advancing blade negative lift, 2) low speed with blade-wake interaction, and 3) high thrust with dynamic stall. The predicted flap bending and torsion moments, pitch link and lag damper loads, in general, show reasonably good correlation with the test data. A nonlinear lag damper model is essential for the accurate prediction of root chord bending moment and lag damper load. Both analyses, however, significantly underpredict the chord bending moments, especially the 4/rev harmonic amplitude. Parametric study shows that blade stiffness variations have only a small influence on the loads calculations. However, modal damping in the first flap mode has a significant influence on the flap bending moments. Inclusion of a simple one degree-of-freedom drivetrain model shows the potential importance of high frequency drivetrain modes for the accurate prediction of the 4/rev chord bending moments and a need to develop a realistic drivetrain model.

NOTATION

A	rotor disk area, πR^2
C_T	rotor thrust coefficient, $T/\rho(\Omega R)^2 A$
C_W	weight coefficient, $GW/\rho(\Omega R)^2 A$
GW	gross weight
L_f	fuselage lift
L_s	stabilator lift
L_{TR}	tail rotor lift
M_x	hub roll moment (positive right down)
M_y	hub pitch moment (positive nose up)
R	rotor radius
T_{MR}	main rotor thrust
V_∞	free-stream velocity
α_s	shaft angle (positive for rearward tilt)
μ	advance ratio, $V_\infty/\Omega R$
ρ	free-stream density
σ	solidity
Ω	rotor angular rotation rate

INTRODUCTION

Accurate prediction of rotor blade loads and vibration is essential for the successful design of rotorcraft. In the design of rotor dynamic components, fatigue life assessment of the components depends heavily on the accuracies of the estimated fatigue design loads (oscillatory rotor loads). Often, these design loads are scaled from previous flight test databases, as calculations are not trustworthy. The rotor loads that are transmitted to the airframe via the rotor hub and swashplate are the dominant source of helicopter vibration. Vibration reduction devices, active and passive, are used to meet very stringent vibration requirements. However, their cost and weight penalty have been excessive in part because of inadequate vibration prediction capability. Accurate prediction capability of rotor loads and vibration at an early design stage has the potential to significantly reduce costly modifications, additional testing, weight penalties, and overall performance degradation.

Rotor loads and vibration analysis is a challenging multidisciplinary problem due to coupling of the complex structural deformations of rotor blades with the three-dimensional and highly unsteady aerodynamic environment. In recent years, there has been significant progress in rotorcraft aeromechanics prediction capability using coupled computational fluid dynamics (CFD) / rotorcraft computational structural dynamics (CSD) analyses (Refs. 1–5). The CFD methods, which use a high fidelity, Navier-Stokes, overset grid methodology with first principles-based wake capturing, overcame the limitations of the conventional lifting line aerodynamics used in rotorcraft comprehensive codes. The CSD methods (through a comprehensive code) performs the sophisticated structural dynamics modeling and also carries out trim calculations. Coupling a CFD code to a comprehensive code marries the strengths of the two approaches and produces the highest fi-

Presented at the AHS 70th Annual Forum, Montréal, Québec, Canada, May 20–22, 2014.

delity solution currently possible.

The present authors demonstrated improved airloads prediction capability using a loosely coupled CFD/CSD method in three challenging level flight conditions of the NASA/Army UH-60A Airloads Program (Ref. 1): 1) high speed, $\mu = 0.37$, $C_T/\sigma = 0.081$ (C8534), with advancing blade negative lift, 2) low speed, $\mu = 0.15$, $C_T/\sigma = 0.076$ (C8513), with blade-wake interaction, and 3) high thrust, $\mu = 0.24$, $C_T/\sigma = 0.129$ (C9017), with dynamic stall. Blade section normal force and pitching moment magnitudes and phases are accurately captured in the coupled solutions, overcoming the inaccuracies of airloads prediction using comprehensive analysis alone. Prediction of rotor airloads for these three flight conditions have been performed by many researchers using various combinations of CFD/CSD tools (Refs. 6–9). All the coupled analyses, in general, show satisfactory airloads correlation with the test data.

Rotor structural loads also have been investigated for these conditions by several researchers (Refs. 10–12). In general, the prediction of the structural loads did not show the same level of correlation with the flight test data as observed for the predicted airloads.

In the present paper, both coupled RCAS (Ref. 13)/Helios (Ref. 14) and CAMRAD II (Ref. 15)/Helios analyses are performed and rotor structural loads results are compared with data from the same three level flight conditions of the NASA/Army UH-60A Airloads Program. Calculated blade flap and chord bending moments, torsion moments, pitch link loads, and lag damper loads are compared with the flight test data. Detailed time history and harmonic responses are examined to assess the high fidelity analysis codes' accuracy in the calculation of rotor structural loads. Effects of a nonlinear damper model, blade stiffness, structural damping, and drive train dynamics on the rotor structural loads are also investigated.

DESCRIPTION OF THE TEST

The test data used in the present study were obtained during the NASA/Army UH-60A Airloads Program conducted from August 1993 to February 1994 (Ref. 16). The database provides aerodynamic pressures, structural loads, control positions, and rotor forces and moments, allowing for the validation of both aerodynamic and structural models. The steady level flight test matrix contains a range of advance ratios and gross weight coefficients as shown in Fig. 1. The three test points investigated here and an aerodynamic rotor lift boundary obtained in wind tunnel testing of a model rotor by McHugh (Ref. 17) are also plotted.

Two of the blades were heavily instrumented: one with subminiature pipette-type pressure transducers and one with a mix of strain-gauges and accelerometers. Absolute pressures were measured at nine radial locations. Blade flap bending, chord bending, and torsion moments were measured with two- or four-leg strain-gauge bridges bonded to the second instrumented blade. The gauges were located at the blade root (11.3% radius) and then evenly distributed along the blade at 10% increments of the rotor radius (20% – 90%). Flap bending moments were measured at all nine radial locations. Chord bending moments were not measured at 90%R and torsion moments were measured only at 30%R, 50%R, 70%R, and 90%R. Additional instrumentation included strain gauges on the pitch links, dampers, and rotor shaft.

All pressure signals were filtered using 550 Hz low-pass 6- pole Butterworth filters and digitized at a rate of 2142 samples/sec/channel. The non-pressure signals were filtered using 110 Hz low-pass 6-pole Butterworth filters and digitized at a rate of 357 samples/sec/channel. For a typical level-flight test condition, a 5 second time slice (approximately 19 revolutions) was stored in the database. These data are stored in the master TRENDS database at the NASA Ames Research Center.

For comparison with analyses, the raw data in the TRENDS database needed to be post-processed. The first step was a zero azimuth reference correction. The zero azimuth reference for the TRENDS database aligned the center of the rotor hub, the center of the elastomeric bearing, points on the blade quarter-chord, and the rotating beacon light on the tail. In order to define the zero azimuth reference to be parallel to the pitch axis, a negative 7-deg blade azimuth shift was applied to all azimuthally dependent data (Ref. 18).

The second step was a correction for the signal delay caused by the antialiasing filters. Assuming an ideal 110 Hz low-pass 6- pole Butterworth filter, the nominal group delay (time shift) of the signal as it goes through the filter is 0.00558 sec (group delays are actually slightly non-linear for this filter type). With the standard flight rotor speed of 258 RPM, this results in an azimuthal delay of approximately 8.6 deg. This azimuthal correction was applied to all the non-pressure channels from the flight test, including the shaft bending gauge. For the 550 Hz filters used for the pressure channels, the equivalent delay was 0.00112 sec, resulting in a correction of 1.7 deg.

The first correction has been applied to the test data since January 2005 (before 2005, the correction was applied in the wrong direction). The second correction was first applied in 2012 for the comparison between the full-scale UH-60A Airloads wind tunnel and flight test data (Ref. 19). For this study, both corrections were applied to the test data.

DESCRIPTION OF ANALYTICAL METHOD

The analytical results were obtained using coupled RCAS/Helios and CAMRAD II/Helios. This section describes each method and how they are coupled to produce a higher fidelity solution.

RCAS and CAMRAD II comprehensive analyses

Rotorcraft Comprehensive Analysis Systems (RCAS) is a comprehensive multidisciplinary, computer software system for predicting rotorcraft aerodynamics, performance, stability

and control, aeroelastic stability, loads, and vibration. RCAS is capable of modeling a wide range of complex rotorcraft configurations operating in hover, forward flight, and maneuvering conditions. The RCAS structural model employs a hierarchical, finite element, multibody dynamics formulation for coupled rotor-body systems. It includes a library of primitive elements including nonlinear beams, rigid body mass, rigid bar, spring, damper, hinges and slides to build arbitrarily complex models. RCAS has been used recently for performance and loads correlation of various rotors including the UH-60A (Refs. 20–22).

Comprehensive Analytical Model of Rotorcraft Aerodynamics and Dynamics (CAMRAD) II is an aeromechanics analysis of rotorcraft that incorporates a combination of advanced technologies including multibody dynamics, nonlinear finite elements, and rotorcraft aerodynamics. CAMRAD II has been used extensively for correlation of performance and loads measurements of the UH-60A in various flight conditions (Refs. 23–26).

Both analyses include multiple aerodynamic options for airloads, wake-induced flow fields, and aerodynamic interference. Airloads models include two-dimensional (2D) airfoil and lifting-line models for rotor blade, wings, and 3D airloads for bodies.

Structural modeling

The UH-60A Black Hawk is modeled in comprehensive analyses as well as CFD as an isolated rotor, not as a complete aircraft. The structural model of the rotor employed in this study is developed from a common UH-60A master input database, which was developed by Yeo and has been used extensively for studies of the UH-60A (Refs. 7, 10, 23, 27). Detailed rotor pitch control system linkage geometry, stiffness, and nonlinear lag damper are also incorporated. To assess the structural dynamic modeling, Ho et al. specified measured airloads from flight test as prescribed external loads and then compared the resulting response with the measured response (Ref. 28). The close agreement between RCAS and CAMRAD II predictions and between the calculations and test data provides significant confidence in the structural dynamics modeling and analysis methodology of the two codes.

Figure 2 compares the blade in-vacuo natural frequencies calculated by RCAS and CAMRAD II. The frequencies shown here are for a nominal zero collective pitch with very small structural damping. The frequency predictions by the two comprehensive codes show good agreement. There are strong couplings between modes for the fourth to sixth modes and participation by each of the contrasting motions depends on the rotor speed for the coupled modes.

Helios

Helicopter Overset Simulations (Helios) is the rotary-wing product of the US Army and CREATE-AV (Air Vehicles) program sponsored by the DoD High Performance Computing Modernization Office (Ref. 14). Helios uses an innovative dual-mesh paradigm that employs unstructured meshes in the "near-body" close to the surface to capture the wall-bounded viscous effects and structured Cartesian grids in the "off-body" to resolve the wake through a combination of higher-order algorithms and adaptive mesh refinement (AMR). An overset procedure facilitates the data exchange and also enables the relative motion between the two meshes. The parallel domain connectivity solver PUNDIT automatically handles the data exchange between the two meshes. CFD is loosely coupled with CSD solvers (RCAS or CAMRAD II) to solve the rotorcraft structural dynamics and trim. A lightweight Python-based software integration framework handles the data exchange between the modules.

The near-body unstructured solver NSU3D is a node-centered, finite-volume-based unsteady Reynolds-Averaged Navier-Stokes (URANS) solver that is spatially second-order accurate and is capable of handling mixed elements. Time-accurate computations utilize a 2nd-order backwards-Euler time stepping scheme along with dual-time stepping for convergence of the nonlinear problem at each physical time step. The Spalart-Allmaras turbulence model is used. The structured solver SAMARC is used for the Cartesian off-body grid system. SAMARC solves the inviscid Euler equations using a 5th-order spatial discretization scheme and 3rd-order explicit Runge-Kutta time integration scheme.

The computational grids model the standard UH-60A blade geometry. The unstructured blade mesh was generated using GRIDGEN and AFLR3 software. The 4 rotor blade grids have 15.4 million nodes and 36.5 million cells. The finest off-body spacing is 5% chord with a fixed refinement region surrounding the rotor plane; AMR is not used here. The off-body grid contains 146 million unblanked grid points on 8 levels. Details of the flow solvers, input parameters, and grids are available in Refs. 4 and 14.

Coupling procedure and trim

The CFD/CSD coupling procedure uses the standard loose or "delta" coupling approach (e.g. Refs. 1 and 2). At each coupling iteration the aerodynamic loads calculated by CFD are passed to CA (Comprehensive Analysis – RCAS or CAMRAD II). After trimming with the CFD airloads, CA computes the blade deflections relative to the blade frame of reference and passes them back to CFD. This sequence is repeated until the airloads, deflections, and control angles converge, typically in about 3-4 revolutions, depending on flight conditions. The exchange of information between CFD and CA codes are handled by the Rotor Fluid Structure Interaction (RFSI) module.

For those cases that looked at the effects of the drivetrain, a modified coupling procedure was used. In particular, it was necessary to return blade deflections from CA in the non-rotating hub frame of reference, so that the drivetrain-induced oscillations would be included in the blade motions. Coordinate system transformations were then applied within Helios

to convert to the blade frame of reference translations and rotations.

An azimuthal step size of 0.1 deg (3600 steps per rotor revolution) was used in the Helios calculations. A 15-deg azimuthal step size, which is standard for the aerodynamic and structural dynamic calculations in CAMRAD II, was used for the high speed and low speed calculations. A 5-deg azimuthal step size was used for the high thrust condition. For the RCAS calculations, a 5-deg azimuthal step size was used for all three conditions.

The comprehensive analysis trim solution for the UH-60A flight-test data solves for the collective and cyclic controls required to obtain the specified rotor thrust and shaft pitch and roll moments with fixed rotor shaft angle. Because there was no direct measure of rotor thrust, it was estimated from known quantities. The procedure is explained below.

The vertical force balance equation is

$$T_{MR}\,cos(\alpha_s) = GW - L_f - L_s - L_{TR} \qquad (1)$$

where T_{MR} is the main rotor thrust, GW is the measured gross weight, L_f is the fuselage lift, L_s is the stabilator lift, and L_{TR} is the lift from the canted tail rotor. The fuselage pitch attitude and stabilator angle were measured on the flight vehicle and the fuselage and stabilator lift curve slopes were obtained from wind tunnel test. The tail rotor lift was estimated from the measured main rotor torque, distance between the main and tail rotors, sideslip angle, and cant angle. This method has been used for the comparison between the small-scale wind tunnel and full-scale flight test data for the UH-60A rotor (Ref. 29). Aircraft moment trim can be specified using the first harmonics of measured hub moments. The rotor hub moment is obtained from the shaft bending moment measured from the strain-gauge bridge.

The trim targets for the three level flight conditions investigated are in Table 1. The coordinate system used is a right hand coordinate system where the x-axis points forward, y right, and z up.

RESULTS AND DISCUSSION

In this section, selected data from the three flight test counters are compared with predictions from the coupled RCAS/Helios and CAMRAD II/Helios analysis methods. These test data include flap and chord bending moments, torsion moments, pitch link loads, and lag damper loads. The analytical results presented in this section are generated using a nonlinear lag damper model, unless otherwise specified.

High speed condition, μ = 0.37, C_T/σ = 0.081 (C8534)

This condition is the maximum-speed counter for the steady level flight test conditions shown in Fig. 1. The rotor blade aerodynamic environment at high speed is characterized by compressibility, negative lift and large aerodynamic pitching moment on the advancing side, with unsteady three-dimensional flows at the tip (Fig. 3).

Figure 4 compares the calculated and measured structural loads. Steady values were removed from both test data and analyses. Figures 4(a), 4(d), and 4(g) show the oscillatory flap bending moments at 30%R, 50%R, and 70%R, respectively. The two coupled analyses agree well with each other and show reasonably good correlation with the flight test data. The peak-to-peak amplitude is well predicted but there is an approximate 10-deg phase difference between the data and analyses.

Figures 4(b), 4(e), and 4(h) show the oscillatory chord bending moments at 11.3%R and 50%R and lag damper load, respectively. Included in these figures are RCAS/Helios predictions using either a linear or nonlinear model of the hydraulic lag damper (the CAMRAD II/Helios predictions use the nonlinear model). The same damper models have been used to study the structural dynamics based on the prescribed airloads, and the damper characteristics are available in Ref. 28. When a nonlinear lag damper model is used, both chord bending moment at 11.3%R and lag damper load are reasonably well predicted. Both models, however, significantly underpredict the magnitude of chord bending moment at 50%R. The effects of the linear lag damper model on the flap bending and torsion moments are small and thus not included in these figures.

Figures 4(c), 4(f), and 4(i) show the oscillatory torsion moments at 30%R and 70%R and pitch link load, respectively. Large aerodynamic pitching moment on the advancing side generates high torsion moments on the blade and pitch link loads on the advancing side. The torsion moment at 30%R (most inboard location) and pitch link loads show very similar waveforms. The analyses show accurate correlation of the torsion moments at 30%R, and thus pitch link loads, in the first and second quadrants. However, the correlation is not satisfactory in the third and fourth quadrants. In general, the torsion moment correlation at 70%R is worse than that at 30%R.

Figure 5 compares the half peak-to-peak amplitude of flap bending, chord bending, and torsion moments along the blade span. The highest flap bending moment occurs at 60%R, with another peak near the blade root (Fig. 5(a)). This peak load is the greatest among the three flight conditions investigated. Although the analyses are able to capture the trends very well, the peak load is underpredicted by about 14%. Chord bending moments are strongly affected by the damper loads, particularly inboard on the blade. The peak load occurs at 30%R and is the greatest among the three flight conditions investigated. The analyses with the nonlinear lag damper model increase the magnitudes and significantly improve the correlation compared to that with the linear model. However, the effect of the nonlinear damper model diminishes around mid span. Unlike the test data, the calculated chord bending moments continually decrease from the blade root to the tip. For this case, the maximum peak loads are underpredicted by about 35%. The half peak-to-peak torsion moments increase from the blade tip to root. The loads show similar magnitude to the high thrust condition (shown later). The analyses show reasonably

good correlation with the test data and slightly underpredict the peak magnitude at 30%R by 6%.

Figure 6 compares the half peak-to-peak and harmonic amplitude of pitch link and lag damper loads. In general, the magnitude decreases as the order of the harmonic increases. The half peak-to-peak pitch link correlation is excellent because the overprediction of the 1/rev harmonic is compensated by the underprediction of 2 and 3/rev harmonic components. The 4/rev harmonic correlation is very good. The lag damper load correlation is reasonably good with the nonlinear lag damper model included. The linear lag damper model significantly underpredicts 1, 2, and 3/rev magnitudes. The overprediction of the half peak-to-peak magnitude (about 5%) is caused by the overprediction of the 3/rev harmonic component.

Figure 7 compares the harmonic magnitude of flap bending, chord bending, and torsion moments along the blade span. In general, lower harmonic components have larger magnitude. The maximum peak locations and shapes differ for each harmonic. The flap bending moment correlation is, in general, very good except for the 3/rev harmonic component. The underprediction of the 3/rev harmonic component is the cause of the underprediction of the peak-to-peak magnitude shown in Fig. 5(a). The measured chord bending moments show a sudden increase of 1/rev harmonic component and a sudden drop of 3/rev harmonic component, although smaller than the 1/rev harmonic, at 40%R and 50%R. The reason for the sudden changes is not known at present. The analyses with the nonlinear lag damper model show much better agreement with the measured data for the 1, 2, and 3/rev harmonics. Lag damper modeling has an important influence near the root of the blade and its effect diminishes around mid span. Even with the nonlinear lag damper model, both analyses significantly underpredict the chord bending moment; the 4/rev harmonic magnitude is particularly poor. The torsion moment correlation is, in general, very good. The measured peak magnitude of the 3/rev harmonic component occurs at 70%R, unlike the rest of the harmonics where the peak magnitude occurs at 30%R. The coupled analyses capture the trends, but significantly underpredict the 3/rev magnitude.

Low speed condition, μ = 0.15, C_T/σ = 0.076 (C8513)

At low speed, the airloads are mainly determined by the interaction between the blades and the vortices trailed from the preceding blades. The airloads measured from the flight test show a sharp “down-up” impulse on the advancing blade and an opposite impulse on the retreating blade near the blade tip (Fig. 8).

Figure 9 compares the calculated and measured structural loads. Again, steady values were removed from both test data and analyses. Figures 9(a), 9(d), and 9(g) show the oscillatory flap bending moments at 30%R, 50%R, and 70%R, respectively. Again, the two coupled analyses agree well with each other. The analyses show reasonably good correlation with the flight test data at 30%R and 50%R. However, the peak-to-peak amplitude is substantially underpredicted at 70%R. The phase difference between the test data and analyses is consistent with the high speed condition.

Figures 9(b), 9(e), and 9(h) show the oscillatory chord bending moments at 11.3%R and 50%R and lag damper load, respectively. Only results with the nonlinear lag damper are shown. Both chord bending moment at 11.3% and lag damper load are overpredicted and the correlation is worse than for the high speed condition. As will be shown later for the high thrust condition, this is the only case that the current analyses show unsatisfactory root chord bending moment and lag damper load correlation. Because of the overall overprediction, the chord bending moment correlation at 50%R appears better compared to the high speed condition.

Figures 9(c), 9(f), and 9(i) show the oscillatory torsion moments at 30%R and 70%R and pitch link load, respectively. As mentioned earlier, the airloads measured from the flight test show a sharp “down-up” impulse on the advancing blade and an opposite impulse on the retreating blade near the blade tip. This impulse is a significant source of negative peak of torsion moments and pitch link loads around 270-deg. The analyses are not able to capture the negative peak on the retreating side.

Figure 10 compares the half peak-to-peak amplitude of flap bending, chord bending, and torsion moments along the blade span. In general, these loads are the smallest among the three flight conditions investigated. The measured flap bending moments show much smaller magnitude at the root than for the high speed condition. The magnitude at 70%R increased by about 60% compared to that at 60%R. The analyses show reasonably good correlation with the measured half peak-to-peak flap bending moments at all the radial locations, except at 70%R. The analyses underpredict the magnitude at 60%R by about 14%, similar to the high speed condition. The measured chord bending moments show almost constant magnitude along the blade span, which is quite a different distribution than that at high speed and high thrust (shown later) conditions. The calculated chord bending moments continually decrease from the blade root to the tip, overpredicting the half peak-to-peak chord bending moments near the root of the blade and significantly underpredicting along the rest of the blade span. The measured half peak-to-peak torsion moments do not decrease from the blade root to tip compared to the high speed and high thrust conditions. The maximum peak occurs at 70%R, unlike the 30%R for the high speed condition. The torsion moment correlation is good at 30%R. However, the analyses significantly underpredict at 70%R and 90%R.

Figure 11 compares the half peak-to-peak and harmonic amplitude of pitch link and lag damper loads. The analyses overpredict the half peak-to-peak pitch link load by about 12%. The 1/rev and 4/rev harmonics are accurately predicted. However, the 2 and 5/rev harmonics are overpredicted and the 3/rev harmonic is underpredicted. As shown in the time history comparison, the lag damper loads are overpredicted at all harmonics, except the 3/rev harmonic component. The analyses overpredict the half peak-to-peak lag damper load by about 35%.

Figure 12 compares the harmonic magnitude of flap bending, chord bending, and torsion moments along the blade span. The flap bending moment correlation is very good except the 3/rev harmonic, where the analyses significantly underpredict. This is consistent with the results at the high speed condition. The underprediction of the 3/rev harmonic component caused slight underprediction of the peak-to-peak magnitude shown in Fig. 10(a).

A recent study using a hybrid method, coupled viscous vortex particle method (VVPM) with CFD/CSD, showed very good correlation of the 3/rev flap bending moment for this condition (Ref. 12). In this method, the CFD solves only the flow field near the blade surface and the VVPM resolves the detailed rotor wake away from the blade surface. Improved wake modeling from the VVPM might be the reason for the accurate prediction of the 3/rev harmonic component. However, the same improvement was not obtained for the high speed and high thrust conditions. Even with the VVPM, the 3/rev flap bending moments were significantly underpredicted for those conditions.

The measured chord bending moments show that the 2/rev harmonic component continues to increase from the blade root to the tip, and both 1 and 3/rev harmonics also increase at 60%R and 70%R. The analyses are not able to predict this trend. The chord bending moment correlation is in general better than the high speed condition. However, the analyses again significantly underpredict the 4/rev magnitude. The measured torsion moments show that the peak magnitudes of both 2 and 3/rev harmonic components occur at 70%R. This explains the maximum half peak-to-peak torsion moment at 70%R shown in Fig. 10(c). The analyses capture this trend for the 2/rev harmonic, but significantly underpredict the 3/rev harmonic because the analyses are not able to capture the negative peak on the retreating side as shown in Figs. 9(c) and 9(f).

High thrust condition, μ = 0.24, C_T/σ = 0.129 (C9017)

This condition is the maximum thrust counter for the steady level flight test conditions. At this high thrust, aerodynamics is dominated by dynamic stall and large negative pitching moment. The measured data show two stall events in the fourth quadrant (Fig. 13).

Figure 14 compares the calculated and measured oscillatory structural loads. Structural loads at some radial locations (e.g. flap and chord bending moments at 50%R) are not available for this flight condition due to strain gauge malfunction. Figures 14(a), 14(d), and 14(g) show the oscillatory flap bending moments at 30%R, 60%R, and 70%R, respectively. The measured flap bending moments at 60%R appear to be band-edged or clipped on the retreating side. The two coupled analyses agree well with each other. As mentioned earlier, a 5-deg azimuthal step size was used in the CAMRAD II calculations for this flight condition. The 15-deg azimuthal step size, which was enough for the high and low speed conditions, was not sufficient for the high-frequency response calculations (mostly 5/rev and above). The number of harmonics used in the solution procedure was increased from the default value of 10 to 16 for convergence and accuracy. The analyses show reasonably good correlation with the flight test data at 30%R. However, the high frequency waveforms and magnitudes are not well captured at 60%R and 70%R.

Figures 14(b), 14(e), and 14(h) show the oscillatory chord bending moments at 11.3%R and 60%R and lag damper load, respectively. The measured chord bending moments at 60%R also appear to be band-edged. Only results with the nonlinear lag damper are shown. Both chord bending moment at 11.3% and lag damper load are well predicted, consistent with the results at the high speed condition. The test data at 60%R show a strong negative peak at 225-deg azimuth. However, the analyses are not able to capture it.

Figures 14(c), 14(f), and 14(i) show the oscillatory torsion moments at 30%R and 70%R and pitch link load, respectively. At high thrust, large pitching moments due to two dynamic stall cycles on the retreating side have an important influence on the blade torsion responses. The measured torsion moments show stronger high frequency content compared to the high speed condition. For example, the torsion moment at 30%R has a large 6/rev component. The analyses show, in general, good correlation but are not able to capture the detailed waveforms.

Figure 15 compares the half peak-to-peak amplitude of flap bending, chord bending, and torsion moments along the blade span. The test data show that the highest flap bending and chord bending moments occur at the blade root, which is quite different from the high and low speed conditions where peak loads occur just outboard of the blade mid span. The analyses capture this trend well. For the flap bending moment, the peak magnitude is underpredicted by about 16%. For the chord bending moment, the peak magnitude is overpredicted by about 10%. The half peak-to-peak torsion moments increase from the blade tip to root. The analyses show reasonably good correlation with the test data and slightly overpredict the peak magnitude at 30%R by about 3%.

Figure 16 compares the half peak-to-peak and harmonic amplitude of pitch link and lag damper loads. The pitch link load in this condition is the greatest among the three flight conditions investigated. The 1 and 5/rev harmonics in this flight condition increased compared to the high speed condition. The analyses underpredict the half peak-to-peak, and 1, 2, and 3/rev harmonic pitch link loads. The analyses overpredict the half peak-to-peak lag damper load by about 9% mainly because of the overprediction of 2 and 5/rev harmonics.

Figure 17 compares the harmonic magnitude of flap bending, chord bending, and torsion moments along the blade span. The flap bending moment correlation is very good except the 3/rev harmonic, where the analyses significantly underpredict. The underprediction of the 3/rev flap bending moment is observed for all three flight conditions investigated. The 1 and 2/rev chord bending moment correlation is reasonably good; much better than the high and low speed correlation. The torsion moment correlation is worse than the high

and low speed conditions, where only 3/rev harmonic component is underpredicted. The analyses underpredict 1/rev harmonic and significantly overpredict 4 and 5/rev harmonics.

Parametric studies of high speed condition

The predicted flap bending moments, in general, show reasonably good correlation with the test data. However, there is the approximate 10-deg phase difference for both high and low speed conditions and the underprediction of 3/rev harmonic for all three flight conditions investigated. Although the nonlinear lag damper model improves the root chord bending moment, the coupled analyses significantly underpredict the peak-to-peak magnitudes, especially the 4/rev harmonic component. To better understand these deficiencies, the effects of blade stiffness, structural damping, and drivetrain dynamics are evaluated at the high speed condition. In these calculations, comprehensive analysis is performed with the final (converged) delta airloads from CFD in order to save computation time. Fully coupled CFD/CSD analyses are carried out selectively and almost identical results are obtained with those with comprehensive analyses using the final delta airloads, confirming that these structural variations do not significantly change airloads.

Figure 18 examines the effects of increasing flap stiffness on the flap bending moments. Flap stiffness values are uniformly increased along the blade span by 10% and 20%, respectively, from the baseline values and the flap bending moment results are compared with the flight test and the baseline results with RCAS/Helios. The flap stiffness variations changed the second flap frequency to 2.86/rev and 2.89/rev, respectively, from the baseline value of 2.84/rev. At 50%R, these variations decrease the minimum peak around 135-deg azimuth and increase the maximum peak around 240-deg azimuth. The harmonic comparison shows that although there is an increase in the 3/rev harmonic, the correlation of 1 and 2/rev harmonics deteriorates.

Figure 19 examines the effects of structural damping on flap bending moments. The baseline analytical model has very small modal damping (0.02% of critical damping) to represent structural damping of the UH-60A blade. The modal damping value is increased to 0.5%, 1.0%, and 2.0%, respectively. Although the same modal damping was applied to all the modes for the results shown here, almost identical results were obtained by applying the modal damping only to the first flap mode. The first flap mode frequency of 1.04/rev is very close to resonance frequency and thus modal damping of this mode strong sensitivity. The structural damping has a significant influence on both magnitude and phase. At 30%R, structural damping tends to smooth out the waveform, eliminating a small hump around 120-deg azimuth. Harmonic comparison shows that structural damping significantly increases 1 and 2/rev harmonic amplitudes and has a small influence on 3/rev harmonic. Structural damping has more influence on the inboard blade section than the outboard section.

Figure 20 examines the effects of chord stiffness and structural damping variations on the chord bending moments at 50%R. Chord stiffness values are uniformly increased along the blade span by 20% and 50%, respectively, from the baseline property. Even with the 50% increase, the chord bending moment does not change much. Again, structural damping tends to smooth out the waveform. Modal damping on the chord modes is not critical because the hydraulic lag damper provides large damping. Although not shown here, the damping value at the pitch bearing has a strong influence on the pitch link loads (but not torsion moments).

The effects of drivetrain dynamics on the chord bending moments are examined next. A simple single-shaft drivetrain model is included in the CAMRAD II analysis (baseline analyses have no drivetrain dynamics). This model is comprised of polar mass moment of inertia, spring stiffness, and damping, and represents one degree-of-freedom torsion dynamics. The effective drivetrain inertia can be considered as the sum of main rotor driveshaft inertia and engine inertia. The effective drivetrain stiffness can be considered as the sum of main rotor driveshaft stiffness and engine driveshaft stiffness. The coupled rotor/drivetrain model captures the effects of the drivetrain on the collective lag modes. The analysis should solve all four blades as the blades are coupled with the drivetrain. As explained earlier, CAMRAD II provides the blade deflections in the non-rotating hub frame and Helios converts them to the deflections in the rotating blade frame. The data passed from Helios to CAMRAD II are airloads data for all four blades.

Various moment of inertia (50, 100, 1000 slug-ft^2) and stiffness values (200000, 300000, 400000 ft-lb/rad) are used to examine their effects on structural loads. Figure 21 shows frequency contents of various dynamic modes that commonly occur in rotorcraft (Ref. 30). Large inertia values used in the parametric study approximate the first drivetrain torsion frequency and small inertial values approximate the second drivetrain torsion frequency. Figure 22 shows the effects of stiffness values on the flap and chord bending moments with a fixed moment of inertia value (1000 slug-ft^2). The results show that the drivetrain changes the phase of both flap and chord bending moments. A smaller stiffness value (softer shaft) generates a slightly larger phase shift. The 10-deg phase difference of flap bending moment is eliminated in the third and the beginning of the fourth quadrants.

Figure 23 shows the effects of moment of inertia values on the flap and chord bending moments with a fixed stiffness value (300000 ft-lb/rad). The changes in moment of inertia do not affect the flap bending moment as shown in Fig. 23(a). However, they have a significant effect on the chord bending moment. The chord bending moment at 50%R in Fig. 23(b) shows that the analyses start to capture the peaks and valleys within the test data and noticeable differences in the waveforms between the test data and the baseline results start to diminish. Figures 23(c) and 23(d) show that there are substantial increases in the half peak-to-peak magnitude and 4/rev harmonic component around the mid span and thus the overall correlation significantly improves.

The results show the potential importance of high fre-

quency drivetrain modes. However, the limitations of the drivetrain model used in the parametric study should be noted. The present single degree-of-freedom model can represent only the fundamental mode of the rotor coupled with a low frequency drive system. Accurate simulation of a high frequency drive system should match both frequency and impedance. Thus, a more complex drive train model, which can capture higher frequency modes, should be developed.

CONCLUSIONS

Structural loads from the NASA/Army UH-60A Airloads Program are compared with calculations obtained using coupled RCAS/Helios and CAMRAD II/Helios analyses at three level flight conditions: 1) high speed, μ = 0.37, C_T/σ = 0.081 (C8534), 2) low speed, μ = 0.15, C_T/σ = 0.076 (C8513), and 3) high thrust, μ = 0.24, C_T/σ = 0.129 (C9017). Calculated blade flap and chord bending moments, torsion moments, pitch link loads, and lag damper loads are compared with the flight test data. From this study the following conclusions are obtained:

1) The two coupled analyses agree well with each other for all three conditions investigated. A 15-deg azimuthal step size in the comprehensive analysis is sufficient for the high and low speed conditions. However, an azimuthal step size of 5 deg is required for the high thrust condition, where high frequency responses are important.

2) The predicted flap bending moments, in general, show reasonably good correlation with the test data. However, there is an approximate 10-deg phase difference for both high and low speed conditions and underprediction of 3/rev harmonic for all three flight conditions investigated.

3) When a nonlinear lag damper model is used, both root chord bending moment and lag damper load are reasonably well predicted. However, the effects of the nonlinear damper model diminishes around mid span. Even with the nonlinear lag damper model, both analyses significantly underpredict the peak-to-peak magnitude of chord bending moments, especially the 4/rev harmonic component.

4) Torsion moment correlation is good except for the underprediction of the 3/rev harmonic magnitude at both high and low speed conditions. However, torsion moment correlation is worse at the high thrust condition. The analyses significantly overpredict both 4 and 5/rev harmonics.

5) Blade stiffness variations have only a small influence on the prediction of flap and chord bending moments. However, modal damping in the first flap mode has a significant influence on the flap bending moments. Large damping values deteriorate the correlation, especially at the inboard blade section.

6) Inclusion of a simple single-shaft drivetrain model shows the potential importance of high frequency drivetrain modes on load predictions. Simulation of the first drivetrain torsion frequency changes the phase of the structural responses. Simulation of the second drivetrain torsion frequency shows a substantial increase in the half peak-to-peak chord bending moment magnitude and the 4/rev harmonic component around the mid span and thus the overall chord bending moment correlation significantly improves. However, due to the limitations of the present simple model, a more complex drive train model, which can capture higher frequency modes, should be developed and incorporated into analyses.

ACKNOWLEDGMENT

The authors gratefully acknowledge Dr. Wayne Johnson at NASA Ames Research Center for many discussions and advice. The authors also acknowledge Dr. Vaidyanathan Anand at the Boeing Company for the valuable discussions on the drivetrain dynamics modeling.

REFERENCES

[1]Potsdam, M., Yeo, H., and Johnson, W., "Rotor Airloads Prediction Using Loose Aerodynamic/Structural Coupling," *Journal of Aircraft*, Vol. 43, (3), May-June 2006, pp. 732-742.

[2]Datta, A., Nixon, M., and Chopra, I., "Review of Rotor Loads Prediction with the Emergence of Rotorcraft CFD," *Journal of the American Helicopter Society*, Vol. 52, (4), October 2007, pp. 287-317.

[3]Bhagwat, M. J., Ormiston, R. A, Saberi, H. A., and Xin, H., "Application of Computational Fluid Dynamics/Computational Structural Dynamics Coupling for Analysis of Rotorcraft Airloads and Blade Loads in Maneuvering Flight," *Journal of the American Helicopter Society*, Vol. 57, (3), April 2012.

[4]Sankaran, V., Potsdam, M., Wissink, A., Datta, A., Jayaraman, B., and Sitaraman, J., "Rotor Loads Prediction in Level and Maneuvering Flight Using Unstructured-Adaptive Cartesian CFD," American Helicopter Society 67th Annual Forum, Virginia Beach, VA, May 3-5, 2011.

[5]Yeo, H., Potsdam, M., and Ormiston, R. A., "Rotor Aeroelastic Stability Analysis Using Coupled Computational Fluid Dynamics/Computation Structural Dynamics," *Journal of the American Helicopter Society*, Vol. 56, (4), October 2011.

[6]Sitaraman, J., Datta, A., Baeder, J., and Chopra, I., "Coupled CFD/CSD prediction of Rotor Aerodynamic and Structural Dynamic Loads for Three Critical Flight Conditions," 31st European Rotorcraft Forum, Florence, Italy, September 13-15, 2005.

[7]Biedron, R. T., and Lee-Rausch, E. M., "Computation of UH-60A Airloads Using CFD/CSD Coupling On Unstructured Meshes," American Helicopter Society 67th Annual Forum, Virginia Beach, VA, May 3-5, 2011.

[8]Rajmohan, N., Marpu, R. P., Sankar, L. N., Baeder, J. D., and Egolf, T. A., "Improved Prediction of Rotor Maneuvering Loads using a Hybrid Methodology," American Helicopter Society 67th Annual Forum, Virginia Beach, VA, May 3-5, 2011.

[9]Zhao, J., and He., C., "Coupled CSD/CFD and Viscous Vortex Particle Method for Rotorcraft Comprehensive Analysis," American Helicopter Society 68th Annual Forum, Fort Worth, TX, May 1-3, 2012.

[10]Datta, A., and Chopra, I., "Prediction of the UH-60A Main Rotor Structural Loads Using Computational Fluid Dynamics/Comprehensive Analysis Coupling," *Journal of the American Helicopter Society*, Vol. 49, (4), October 2008, pp. 351-365.

[11]Opoku, D., Makinen, S. M., and Wake, B. E., "Investigation of Loose and Tight Aeroelastic Coupling for High Speed and High Thrust Flight Conditions," American Helicopter Society 67th Annual Forum, Virginia Beach, VA, May 3-5, 2011.

[12]Zhao, J., and He., C., "Rotor Blade Structural Loads Analysis Using Coupled CSD/CFD/VVPM," American Helicopter Society 69th Annual Forum, Phoenix, AZ, May 21-23, 2013.

[13]Saberi, H. A., Khoshlahjeh, M., Ormiston, R. A., and Rutkowski, M. J., "RCAS Overview and Application to Advanced Rotorcraft Problems," AHS Fourth Decennial Specialists' Conference on Aeromechanics, San Francisco, CA, January 21-23, 2004.

[14]Sankaran, V., Wissink, A., Datta, A., Sitaraman, J., Jayaraman, B., Potsdam, M., Kamkar, S., Katz, A., Mavriplis, D., Roget, B., Saberi, H., Chen, W.-B., Johnson, W., and Strawn, R., "Overview of the Helios Version 2.0 Computational Platform for Rotorcraft Simulations," 48th AIAA Aerospace Sciences Meeting Including the New Horizons Forum and Aerospace Exposition, Orlando, FL, January 4-7, 2010.

[15]Johnson, W., "Technology Drivers in the Development of CAMRAD II," American Helicopter Society Aeromechanics Specialist Meeting, San Francisco, CA, January 19-21, 1994.

[16]Bousman, W. G., and Kufeld, R. M., "UH-60A Airloads Catalog," NASA TM-2005-212827, August 2005.

[17]McHugh, F. J., Clark, R., and Solomon, M., "Wind Tunnel Investigation of Rotor Lift and Propulsive Force at High Speed - Data Analysis," NASA CR 145217-1, October 1977.

[18]Kufeld, R. M., and Bousman, W. G., "UH-60A Airloads Program Azimuth Reference Correction," *Journal of the American Helicopter Society*, Vol. 50, (2), April 2005, pp. 211-213.

[19]Norman, T., R., Peterson, R. L., Maier, T., H., and Yeo, H., "Evaluation of Wind Tunnel and Scaling Effects with the UH-60A Airloads Rotor," American Helicopter Society 68th Annual Forum, Fort Worth, TX, May 1-3, 2012.

[20]Jain, R., Yeo, H., Bhagwat, M., and Ho, J. C., "An Assessment of RCAS Performance Prediction for Conventional and Advanced Rotor Configurations," American Helicopter Society 70th Annual Forum, Montréal, Québec, Canada, May 20-22, 2013.

[21]Wachspress, D. A., Yu, K., Saberi, H., Hasbun, M. J., Ho, J. C., and Yeo, H., "Comprehensive Analysis Predictions of Helicopter Rotor Airloads using a Fast Loose-Coupled Aerodynamics Solution," American Helicopter Society 68th Annual Forum, Fort Worth, TX, May 1-3, 2012.

[22]Yu, K., Wachspress, D. A., Saberi, H., Hasbun, M. J., Ho, J. C., and Yeo, H., "Comprehensive Analysis Predictions of Helicopter Rotor Structural Loads using a Fast Loose-Coupled Aerodynamics Solution," American Helicopter Society 68th Annual Forum, Fort Worth, TX, May 1-3, 2012.

[23]Yeo, H., Bousman, W. G., and Johnson, W., "Performance Analysis of a Utility Helicopter with Standard and Advanced Rotor," *Journal of the American Helicopter Society*, Vol. 53, (3), July 2004, pp. 250-270.

[24]Shinoda, P. M., Yeo. H., and Norman, T. R., "Rotor Performance of a UH-60 Rotor System in the NASA Ames 80- by 120-Foot Wind Tunnel," *Journal of the American Helicopter Society*, Vol. 49, (4), October 2004, pp. 401-413.

[25]Yeo, H., and Johnson, W., "Assessment of Comprehensive Analysis Calculation of Airloads on Helicopter Rotors," *Journal of Aircraft*, Vol. 42, (5), September-October 2005, pp. 1218-1228.

[26]Yeo, H., and Johnson, W., "Prediction of Rotor Structural Loads with Comprehensive Analysis," *Journal of the American Helicopter Society*, Vol. 53, (2), April 2008, pp. 193-209.

[27]Ormiston, R. A., "An Investigation of the Mechanical Airloads Problem for Evaluating Rotor Blade Structural Dynamics Analysis," American Helicopter Society 4th Decennial Specialists' Conference on Aeromechanics, San Francisco, CA, January 21-23, 2004.

[28]Ho, J. C., Yeo, H., and Ormiston, R. A., "Investigation of Rotor Blade Structural Dynamics and Modeling Based on Measured Airloads," *Journal of Aircraft*, Vol. 45, No. 5, September-October 2008, pp. 1631-1642.

[29]Tung, C., Bousman, W. G., and Low, S., "A Comparison of Airload Data Between Model-Scale Rotor and Full-Scale Flight Test," American Helicopter Society Aeromechanics and Product Design, Bridgeport, CT, October 11-13, 1995.

[30]Mihaloew, J. R., Ballin, M. G., and Ruttledge, D. C. G., "Rotorcraft Flight-Propulsion Control Integration: An Eclectic Design Concept," NASA TP 2815, April 1988.

Table 1. Rotor trim conditions

Counter	μ	C_T/σ	α_s	M_x, ft-lb	M_y, ft-lb
C8534	0.37	0.081	$-7.31°$	-5350	-5025
C8513	0.15	0.076	$0.75°$	-129	-5552
C9017	0.24	0.129	$-0.15°$	-354	-193

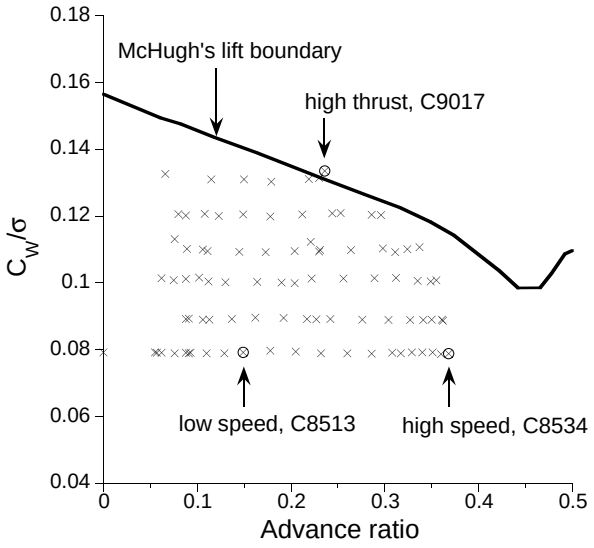

Fig. 1. UH-60A Airloads Program level flight test matrix.

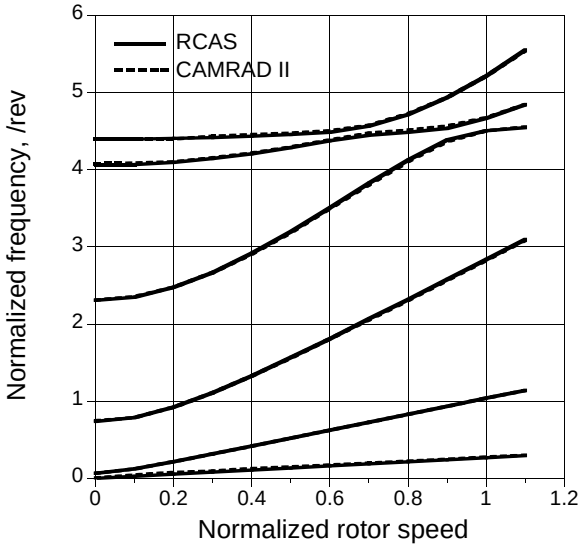

Fig. 2. Rotor blade natural frequency comparison.

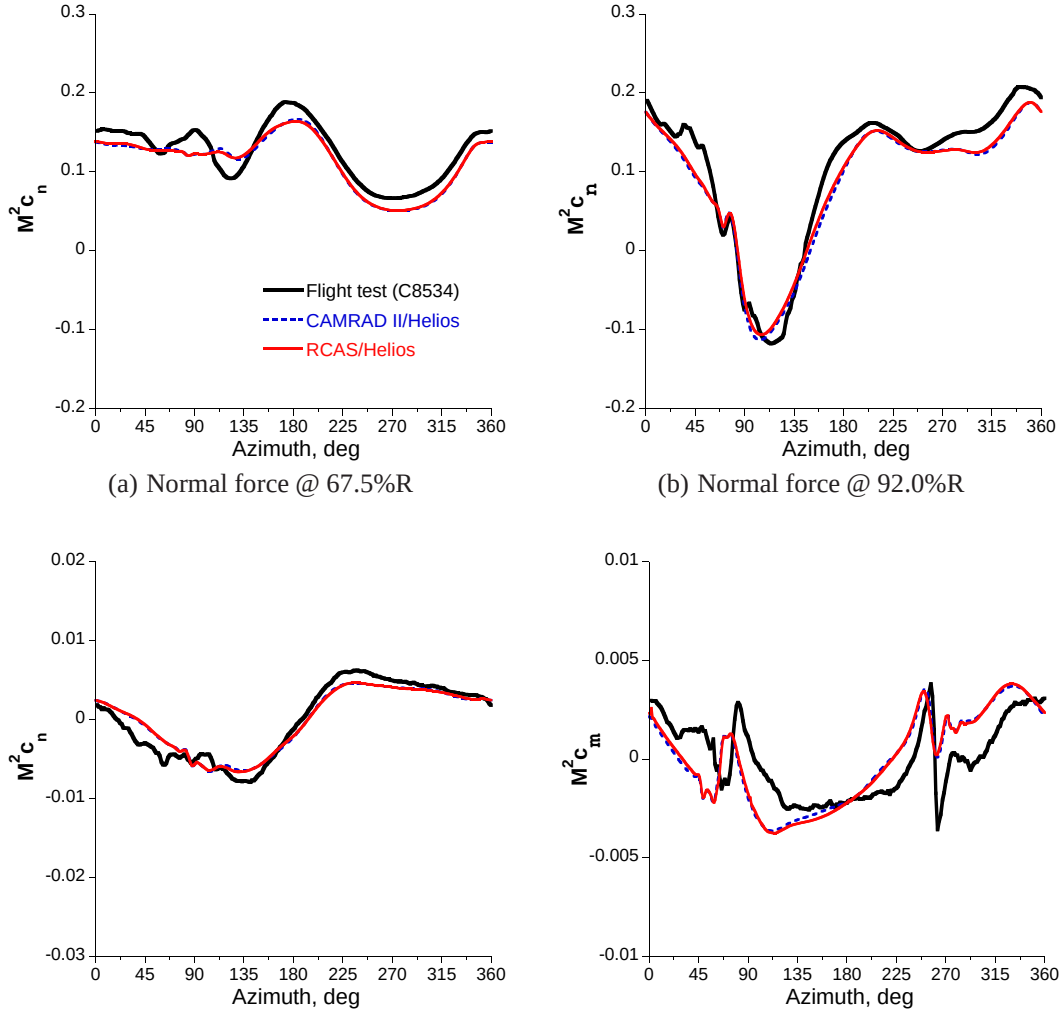

(a) Normal force @ 67.5%R

(b) Normal force @ 92.0%R

(c) Pitching moment @ 67.5%R (mean removed)

(d) Pitching moment @ 92.0%R (mean removed)

Fig. 3. Blade section normal force and pitching moment, μ = 0.37, C_T/σ = 0.081 (C8534).

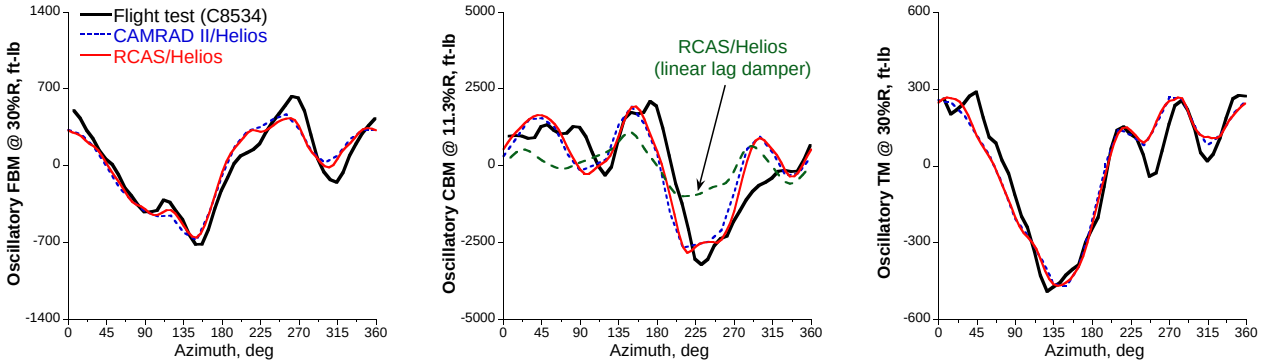

(a) Flap bending moment @ 30%R

(b) Chord bending moment @ 11.3%R

(c) Torsion moment @ 30%R

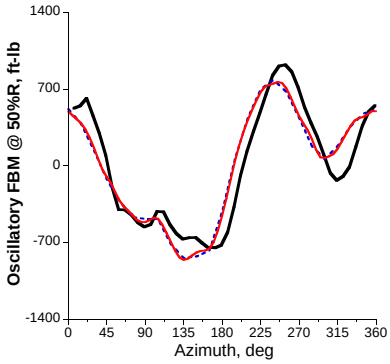

(d) Flap bending moment @ 50%R

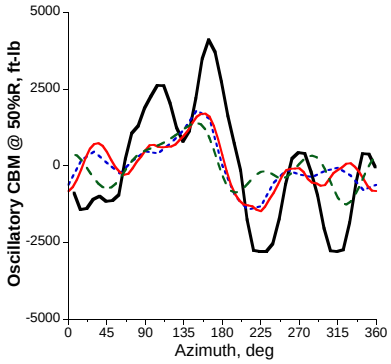

(e) Chord bending moment @ 50%R

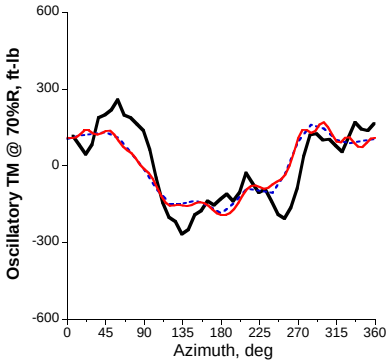

(f) Torsion moment @ 70%R

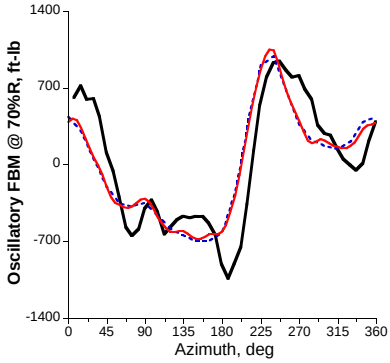

(g) Flap bending moment @ 70%R

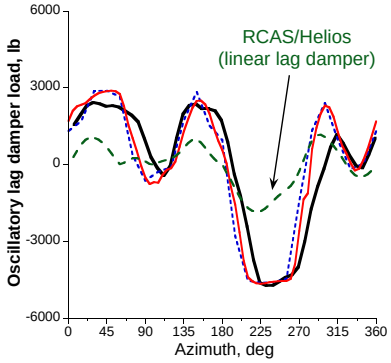

(h) Lag damper load

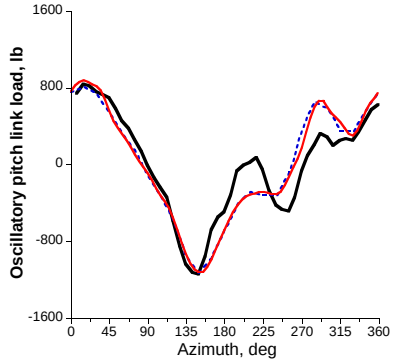

(i) Pitch link load

Fig. 4. Comparison of time history of calculated and measured structural loads, μ = 0.37, C_T/σ = 0.081 (C8534).

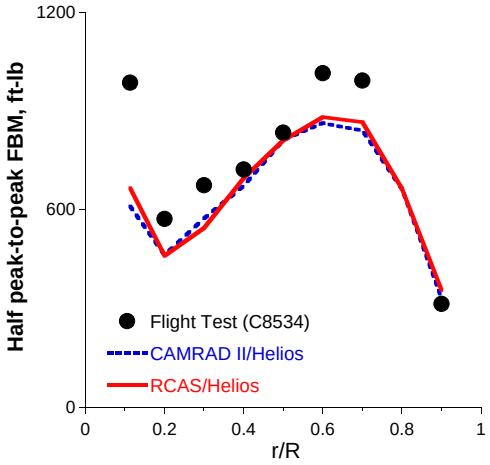

(a) Flap bending moment

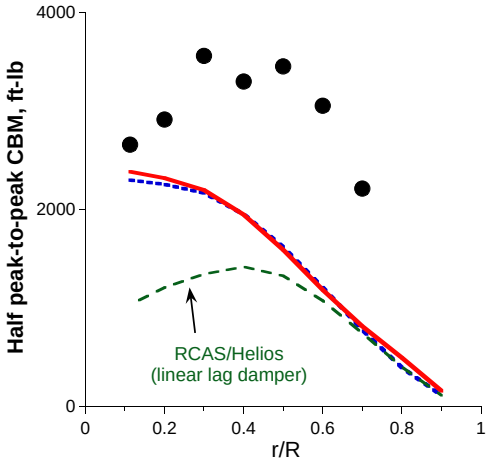

(b) Chord bending moment

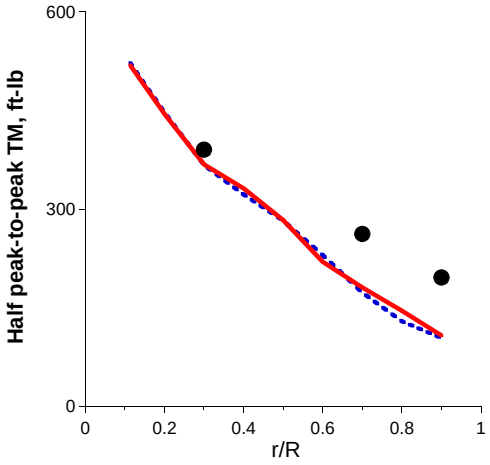

(c) Torsion moment

Fig. 5. Comparison of half peak-to-peak magnitude of calculated and measured blade structural loads, μ = 0.37, C_T/σ = 0.081 (C8534).

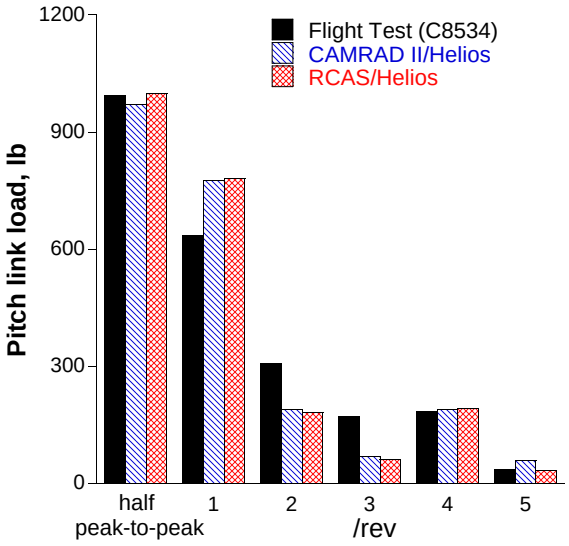

(a) Pitch link load

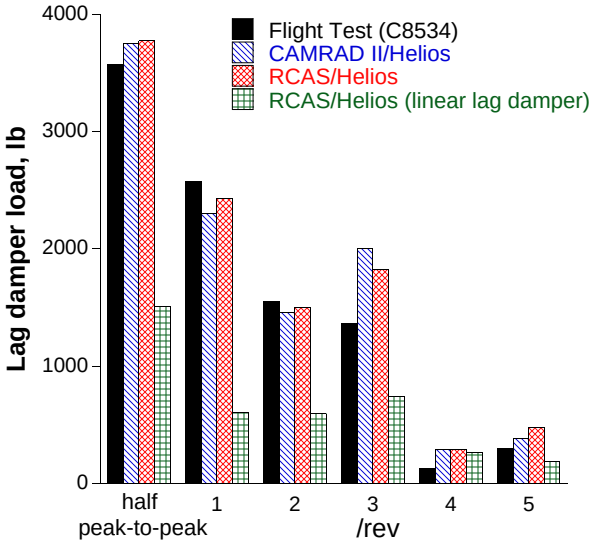

(b) Lag damper load

Fig. 6. Comparison of half peak-to-peak and harmonic magnitude of calculated and measured pitch link and damper loads, μ = 0.37, C_T/σ = 0.081 (C8534).

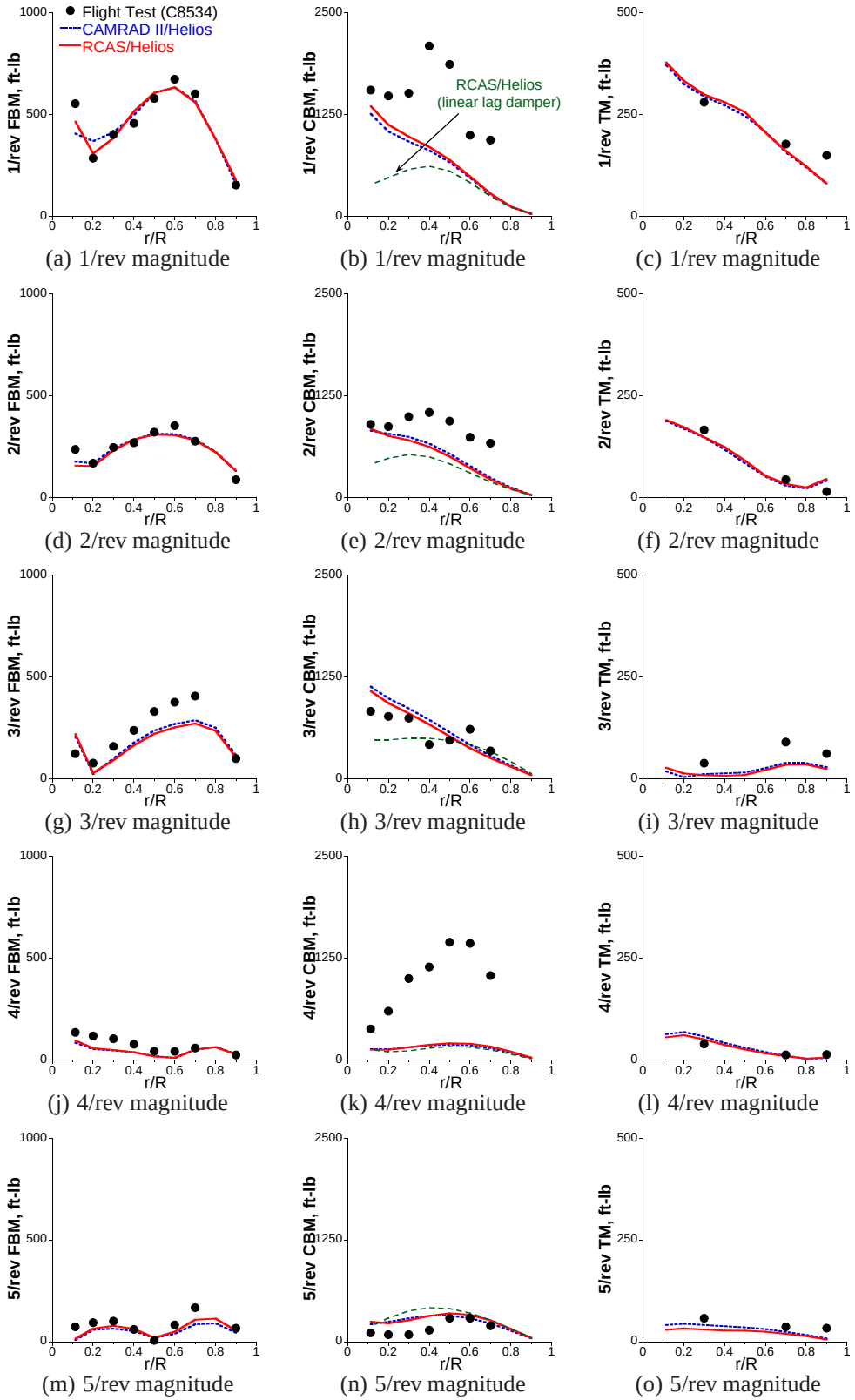

(a) 1/rev magnitude (b) 1/rev magnitude (c) 1/rev magnitude

(d) 2/rev magnitude (e) 2/rev magnitude (f) 2/rev magnitude

(g) 3/rev magnitude (h) 3/rev magnitude (i) 3/rev magnitude

(j) 4/rev magnitude (k) 4/rev magnitude (l) 4/rev magnitude

(m) 5/rev magnitude (n) 5/rev magnitude (o) 5/rev magnitude

Fig. 7. Comparison of harmonic magnitude of calculated and measured structural loads, μ = 0.37, C_T/σ = 0.081 (C8534).

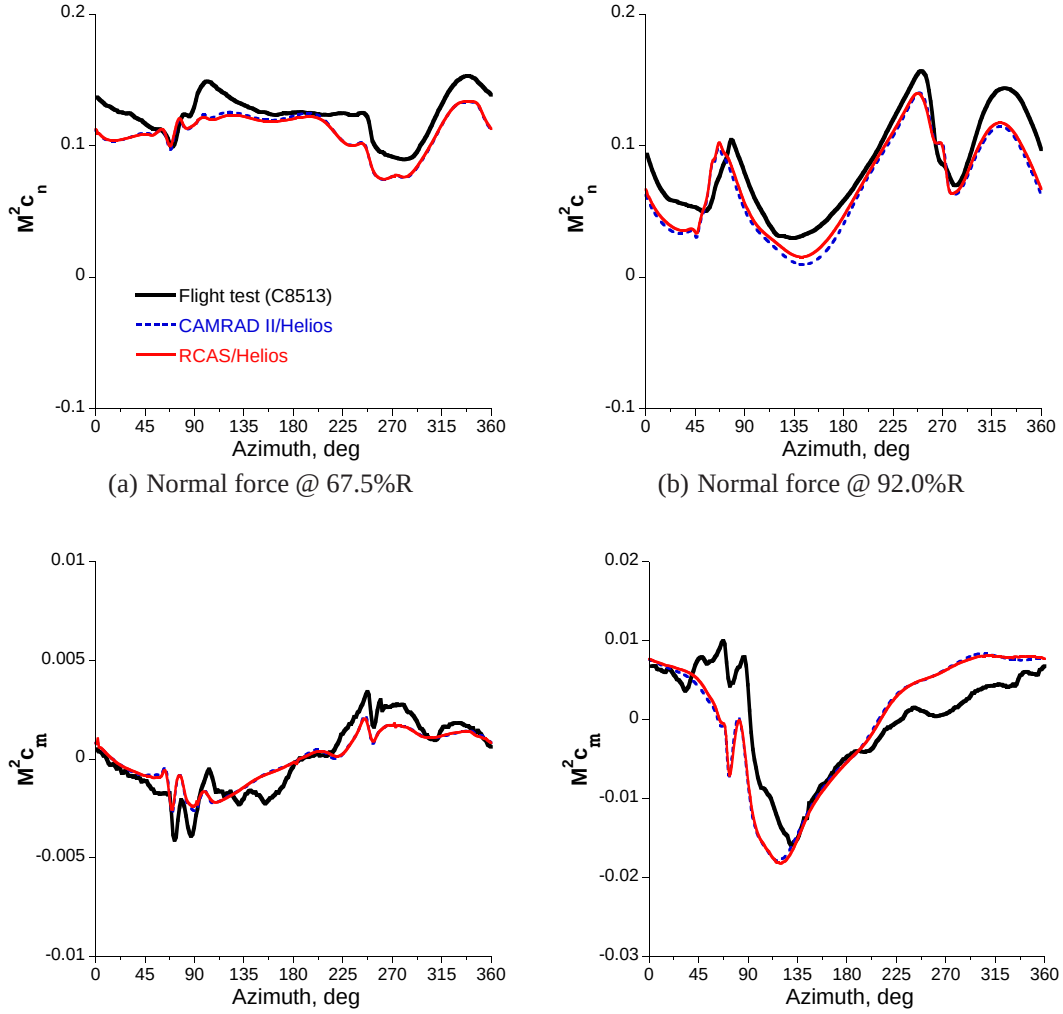

(a) Normal force @ 67.5%R

(b) Normal force @ 92.0%R

(c) Pitching moment @ 67.5%R (mean removed)

(d) Pitching moment @ 92.0%R (mean removed)

Fig. 8. Blade section normal force and pitching moment, μ = 0.15, C_T/σ = 0.076 (C8513).

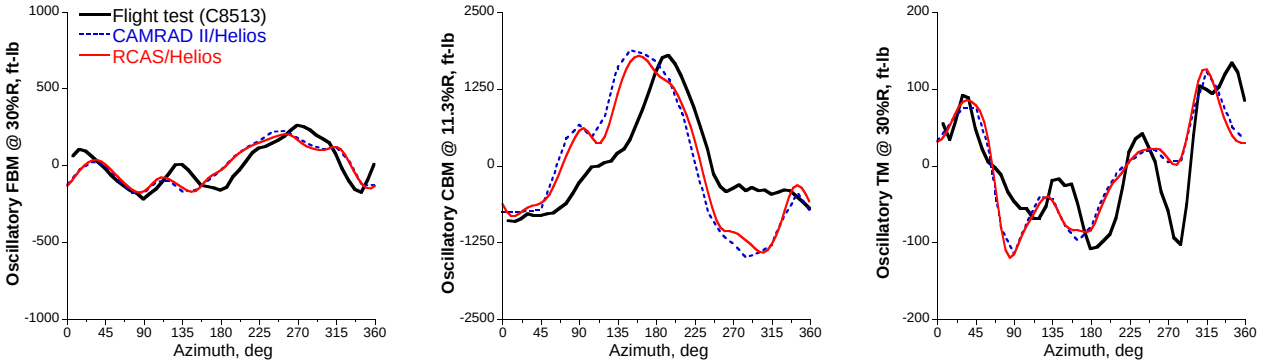

(a) Flap bending moment @ 30%R (b) Chord bending moment @ 11.3%R (c) Torsion moment @ 30%R

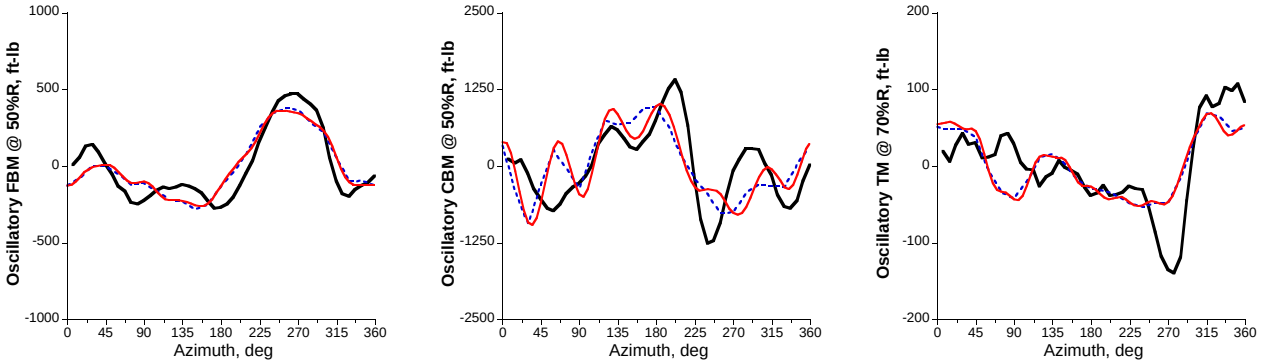

(d) Flap bending moment @ 50%R (e) Chord bending moment @ 50%R (f) Torsion moment @ 70%R

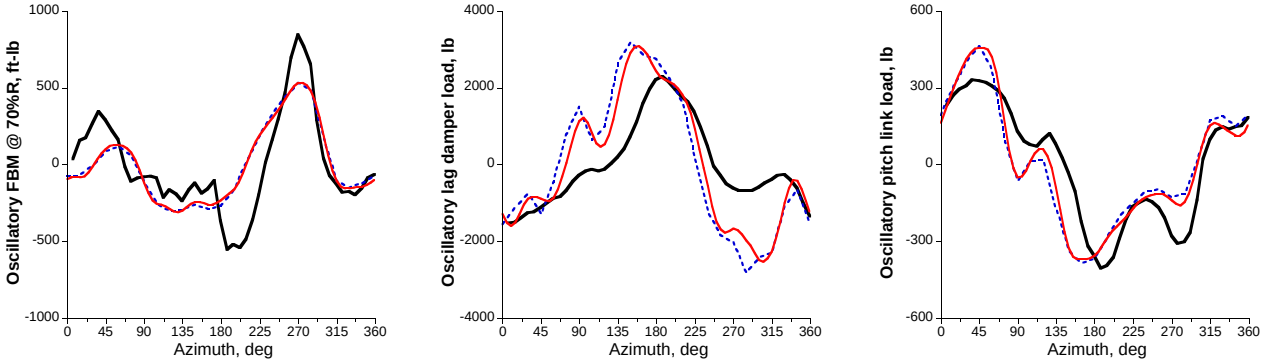

(g) Flap bending moment @ 70%R (h) Lag damper load (i) Pitch link load

Fig. 9. Comparison of time history of calculated and measured structural loads, μ = 0.15, C_T/σ = 0.076 (C8513).

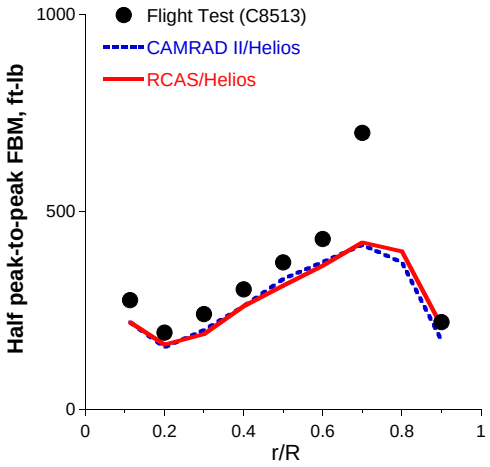

(a) Flap bending moment

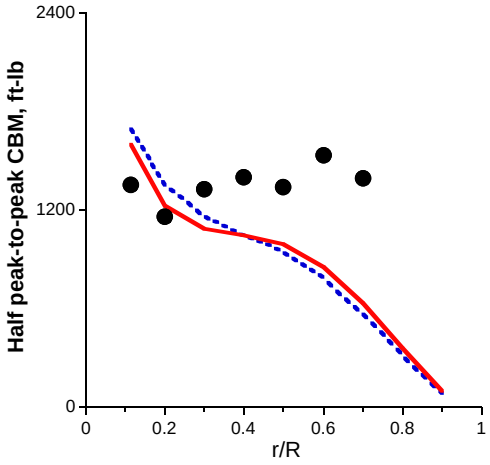

(b) Chord bending moment

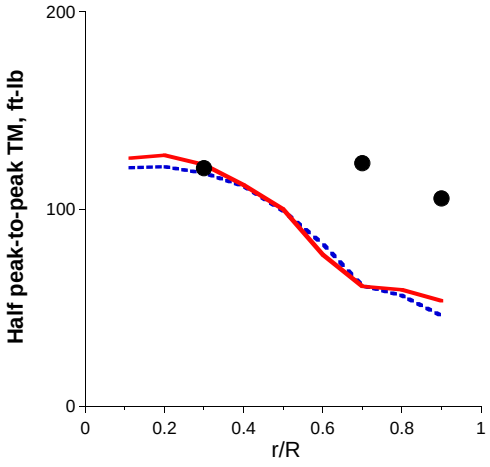

(c) Torsion moment

Fig. 10. Comparison of half peak-to-peak magnitude of calculated and measured blade structural loads, μ = 0.15, C_T/σ = 0.076 (C8513).

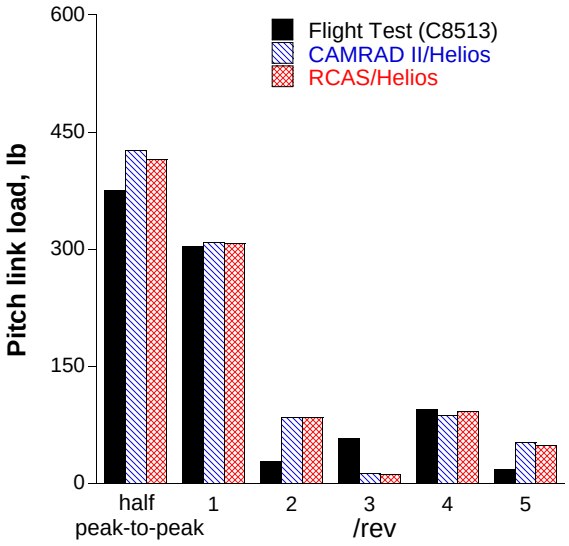

(a) Pitch link load

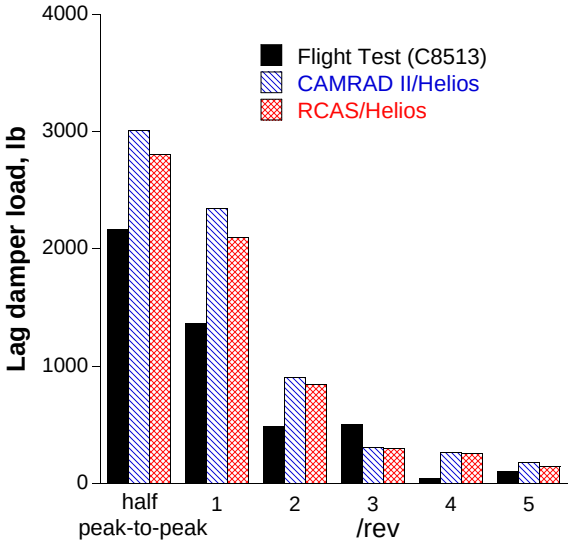

(b) Lag damper load

Fig. 11. Comparison of half peak-to-peak and harmonic magnitude of calculated and measured pitch link and damper loads, μ = 0.15, C_T/σ = 0.076 (C8513).

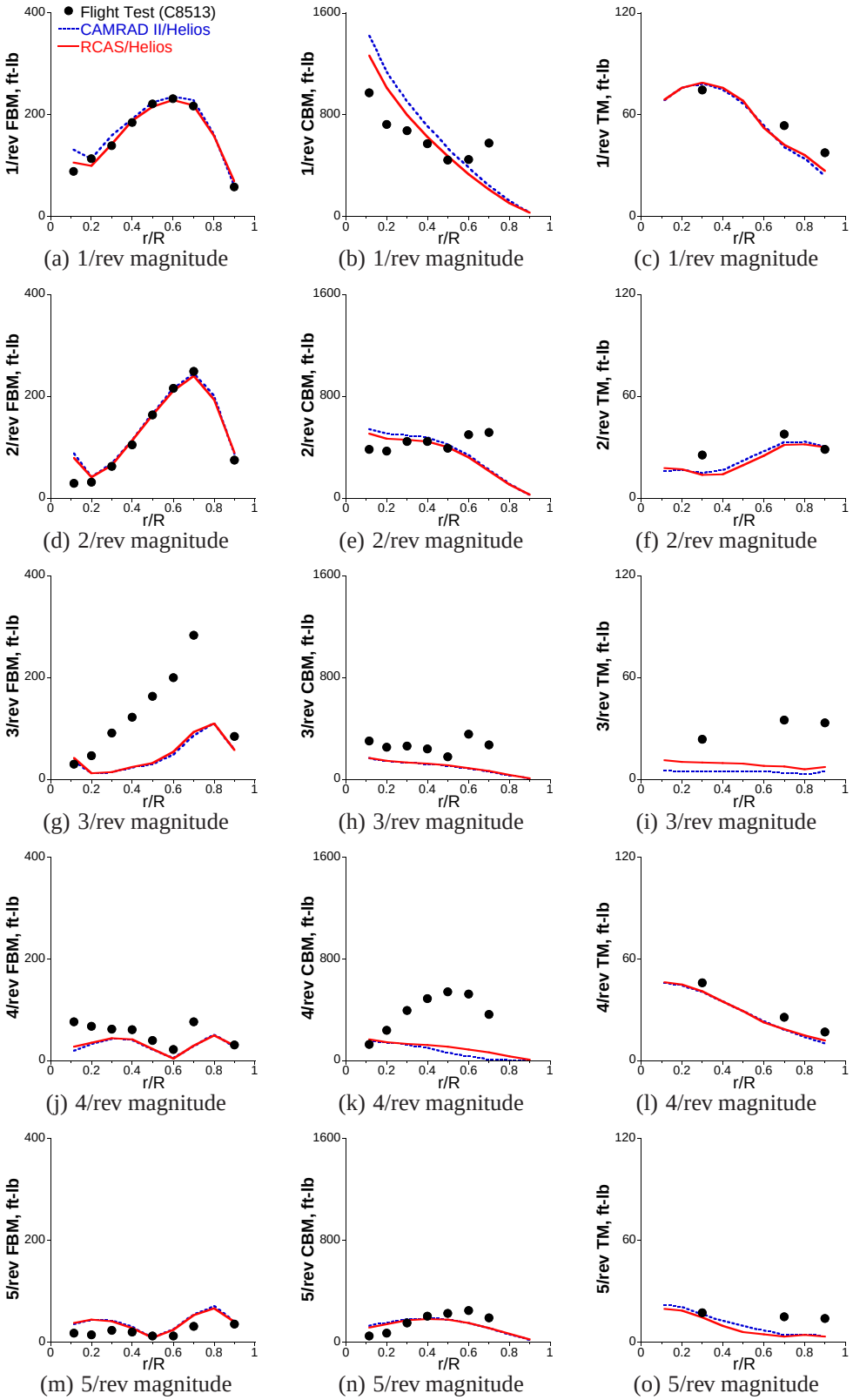

(a) 1/rev magnitude (b) 1/rev magnitude (c) 1/rev magnitude

(d) 2/rev magnitude (e) 2/rev magnitude (f) 2/rev magnitude

(g) 3/rev magnitude (h) 3/rev magnitude (i) 3/rev magnitude

(j) 4/rev magnitude (k) 4/rev magnitude (l) 4/rev magnitude

(m) 5/rev magnitude (n) 5/rev magnitude (o) 5/rev magnitude

Fig. 12. Comparison of harmonic magnitude of calculated and measured structural loads, μ = 0.15, C_T/σ = 0.076 (C8513).

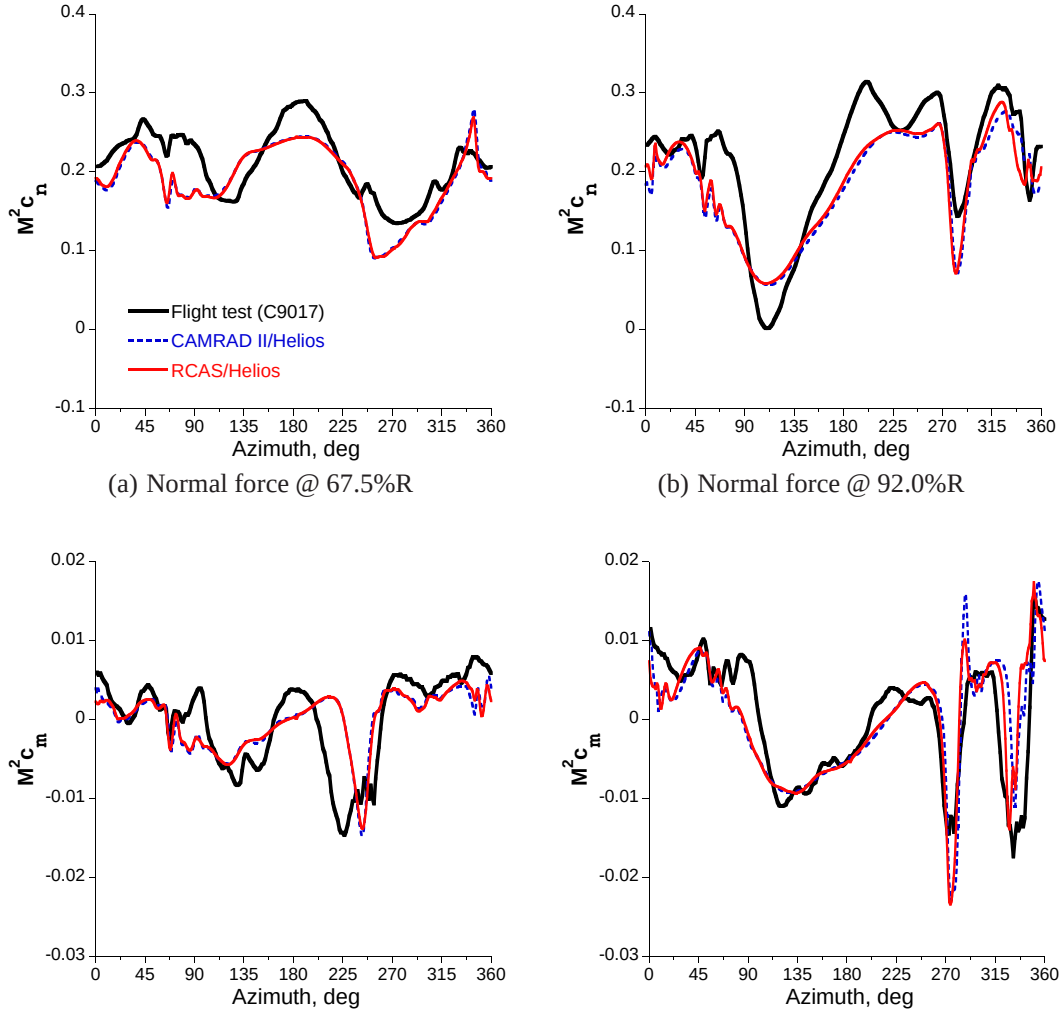

(a) Normal force @ 67.5%R

(b) Normal force @ 92.0%R

(c) Pitching moment @ 67.5%R (mean removed)

(d) Pitching moment @ 92.0%R (mean removed)

Fig. 13. Blade section normal force and pitching moment, μ = 0.24, C_T/σ = 0.129 (C9017).

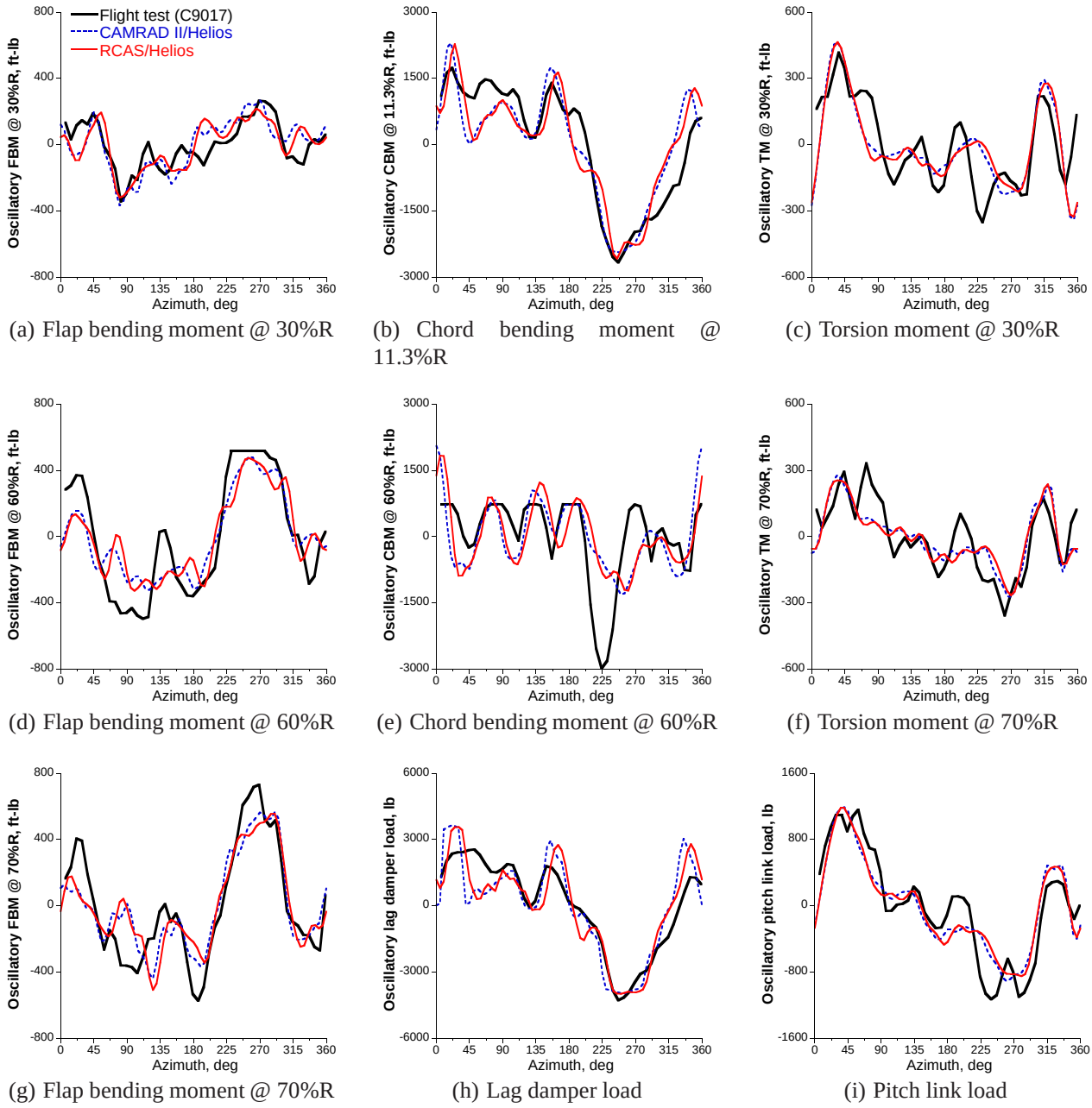

(a) Flap bending moment @ 30%R (b) Chord bending moment @ 11.3%R (c) Torsion moment @ 30%R

(d) Flap bending moment @ 60%R (e) Chord bending moment @ 60%R (f) Torsion moment @ 70%R

(g) Flap bending moment @ 70%R (h) Lag damper load (i) Pitch link load

Fig. 14. Comparison of time history of calculated and measured structural loads, μ = 0.24, C_T/σ = 0.129 (C9017).

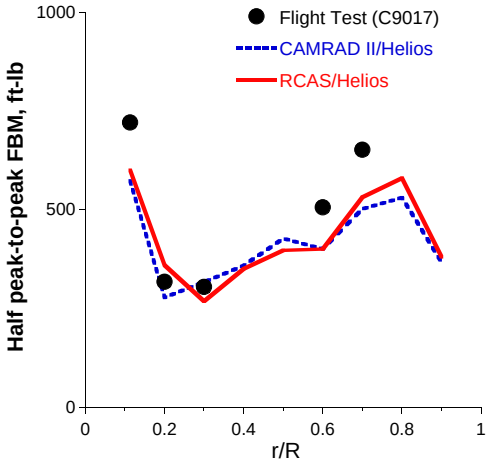

(a) Flap bending moment

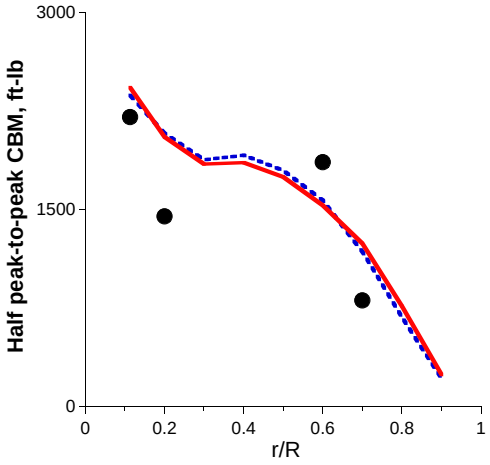

(b) Chord bending moment

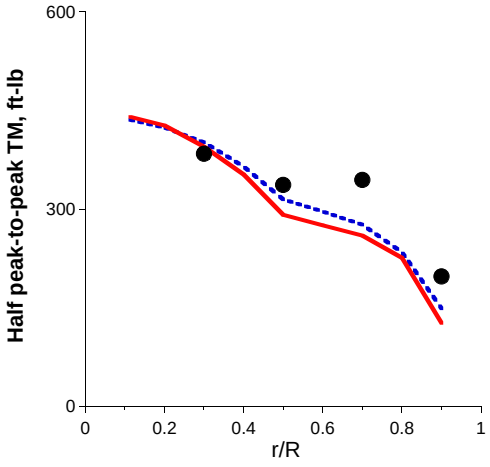

(c) Torsion moment

Fig. 15. Comparison of half peak-to-peak magnitude of calculated and measured blade structural loads, μ = 0.24, C_T/σ = 0.129 (C9017).

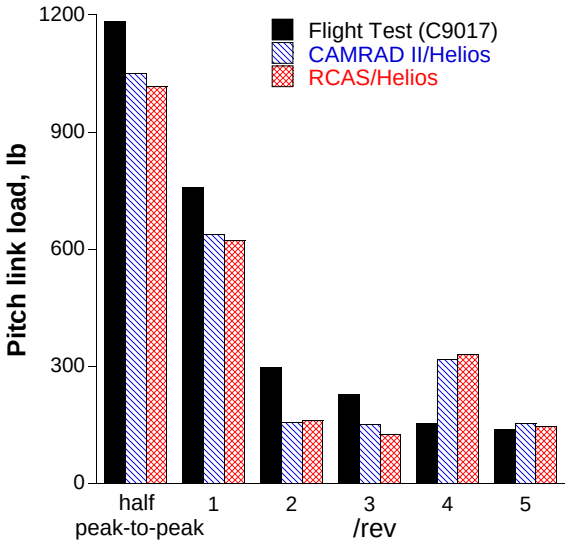

(a) Pitch link load

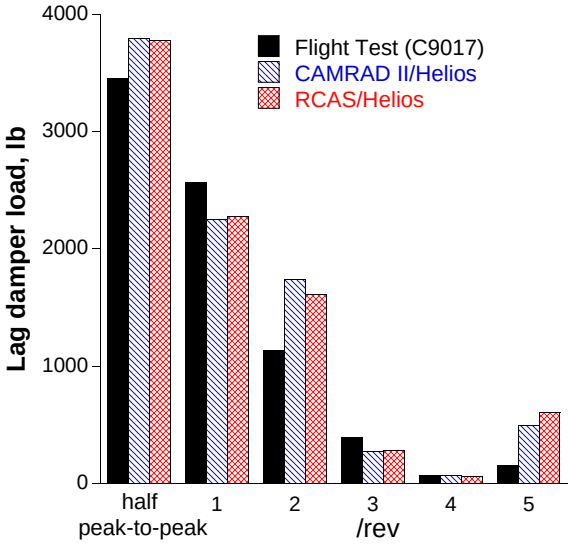

(b) Lag damper load

Fig. 16. Comparison of half peak-to-peak and harmonic magnitude of calculated and measured pitch link and damper loads, μ = 0.24, C_T/σ = 0.129 (C9017).

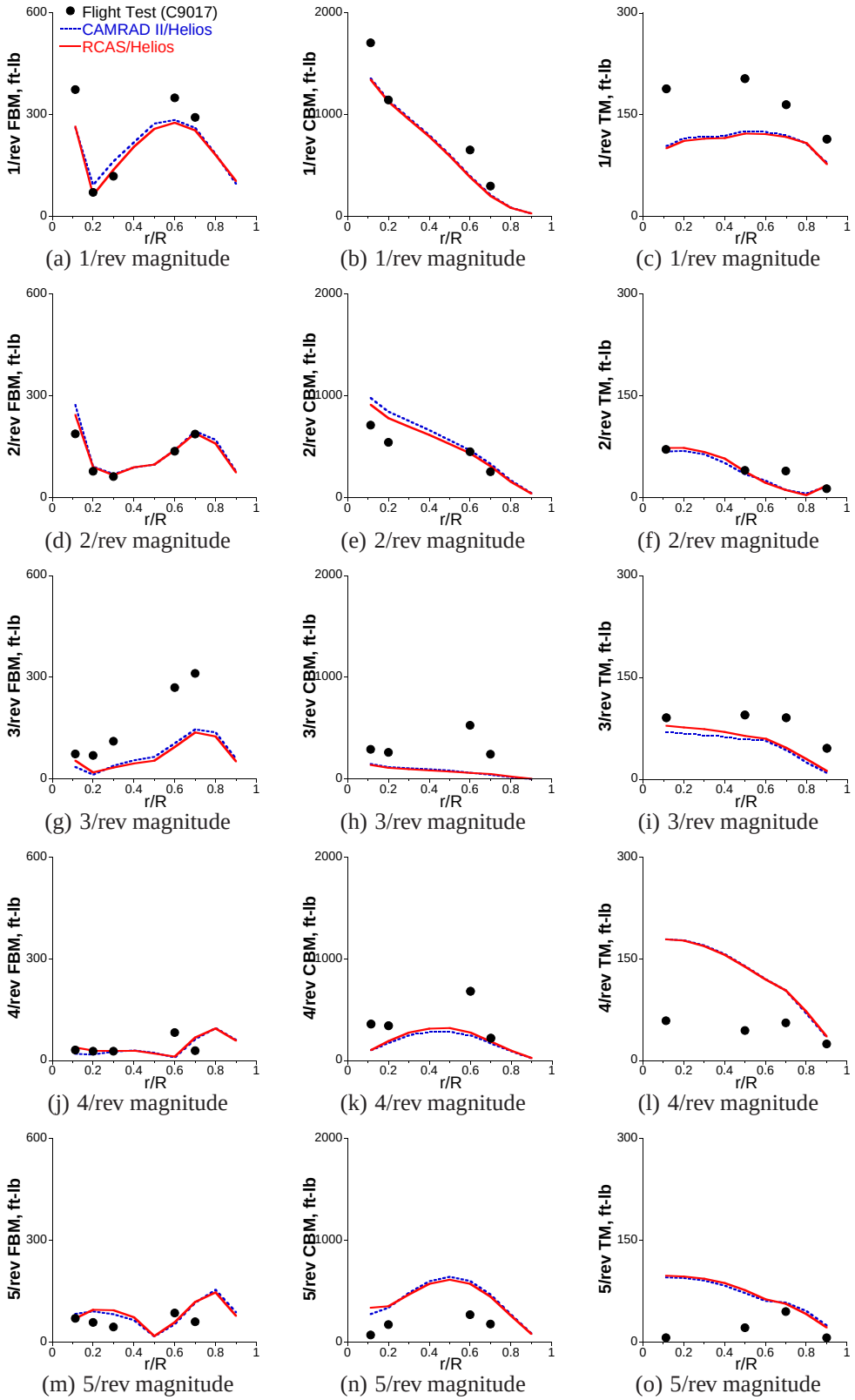

(a) 1/rev magnitude (b) 1/rev magnitude (c) 1/rev magnitude

(d) 2/rev magnitude (e) 2/rev magnitude (f) 2/rev magnitude

(g) 3/rev magnitude (h) 3/rev magnitude (i) 3/rev magnitude

(j) 4/rev magnitude (k) 4/rev magnitude (l) 4/rev magnitude

(m) 5/rev magnitude (n) 5/rev magnitude (o) 5/rev magnitude

Fig. 17. Comparison of harmonic magnitude of calculated and measured structural loads, μ = 0.24, C_T/σ = 0.129 (C9017).

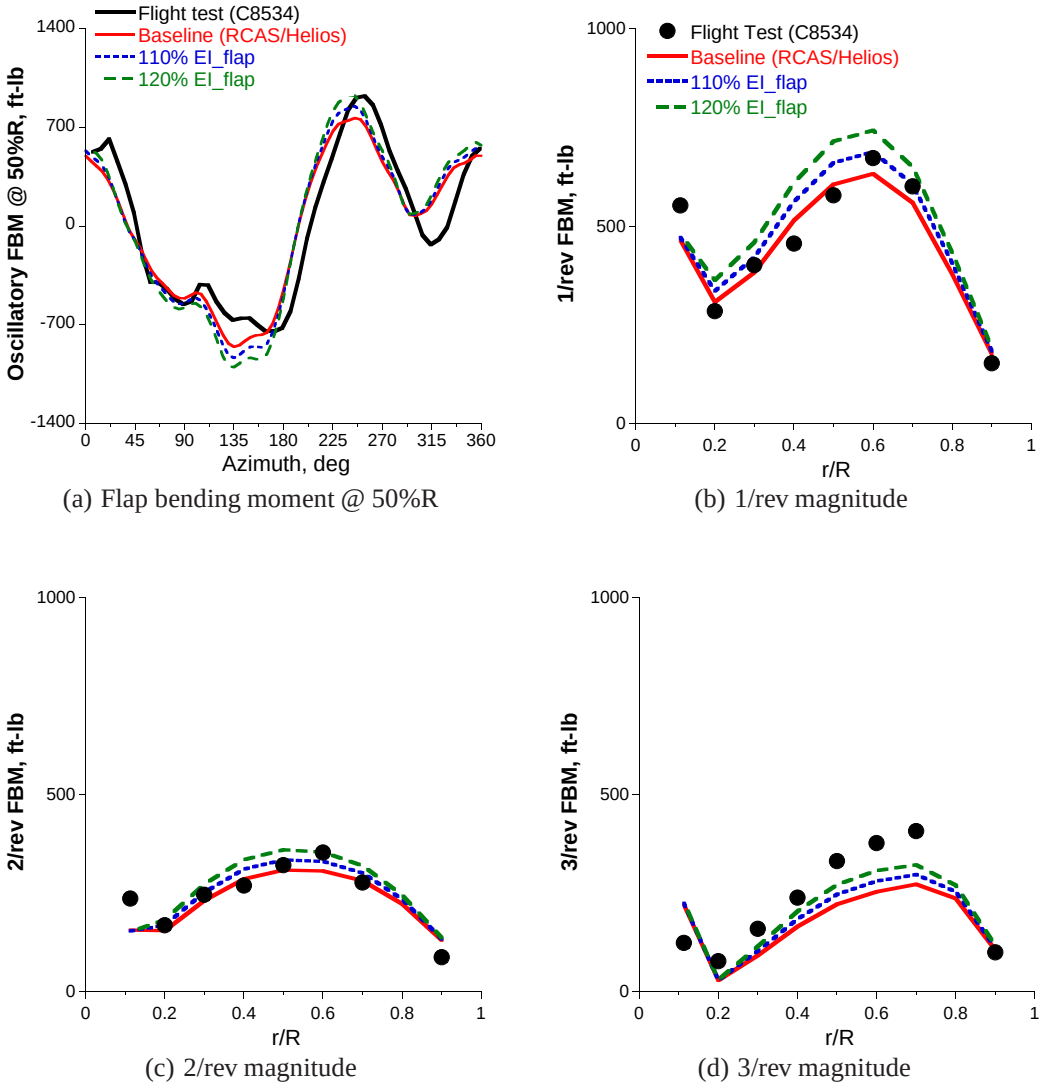

(a) Flap bending moment @ 50%R

(b) 1/rev magnitude

(c) 2/rev magnitude

(d) 3/rev magnitude

Fig. 18. Effects of flap stiffness on flap bending moments, μ = 0.37, C_T/σ = 0.081 (C8534).

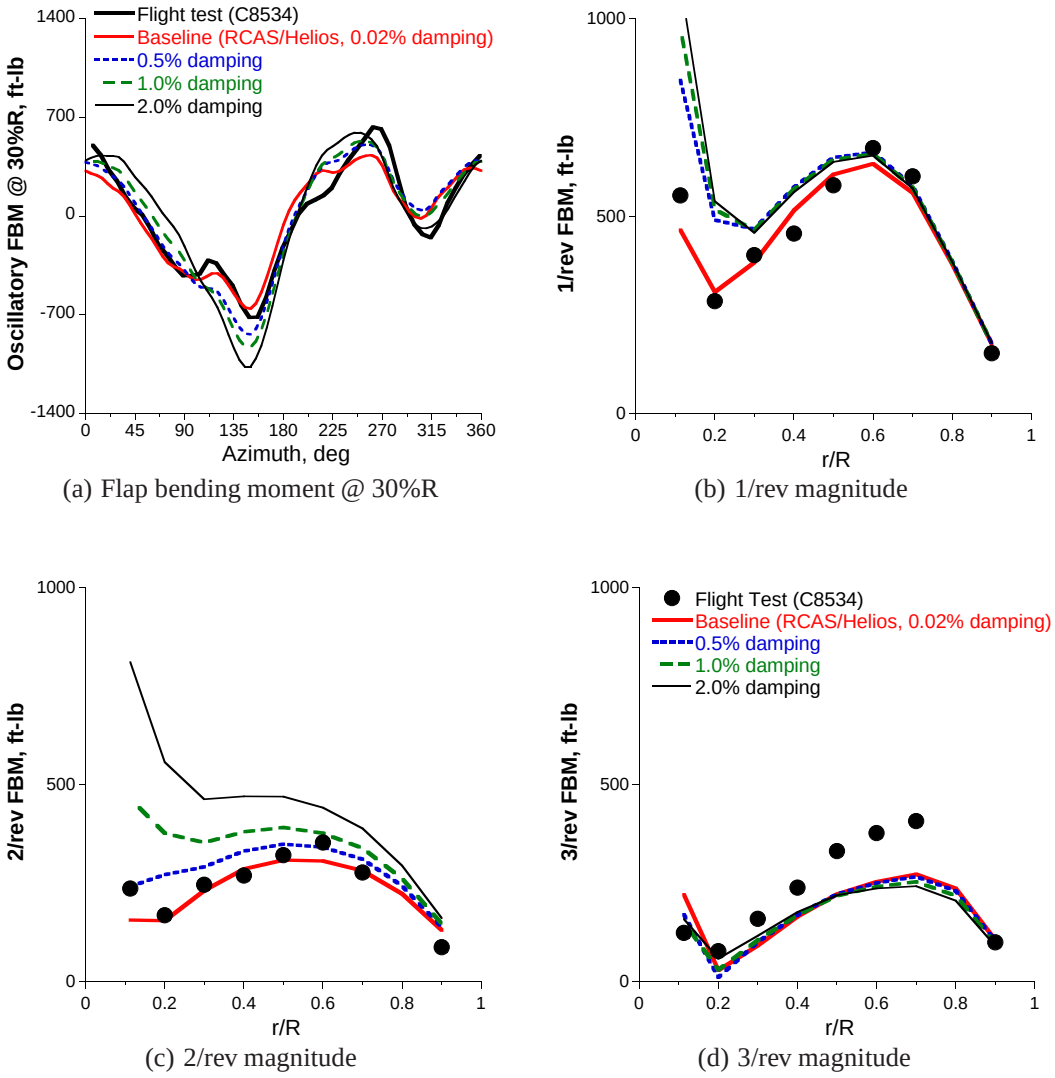

(a) Flap bending moment @ 30%R

(b) 1/rev magnitude

(c) 2/rev magnitude

(d) 3/rev magnitude

Fig. 19. Effects of structural damping on flap bending moments, μ = 0.37, C_T/σ = 0.081 (C8534).

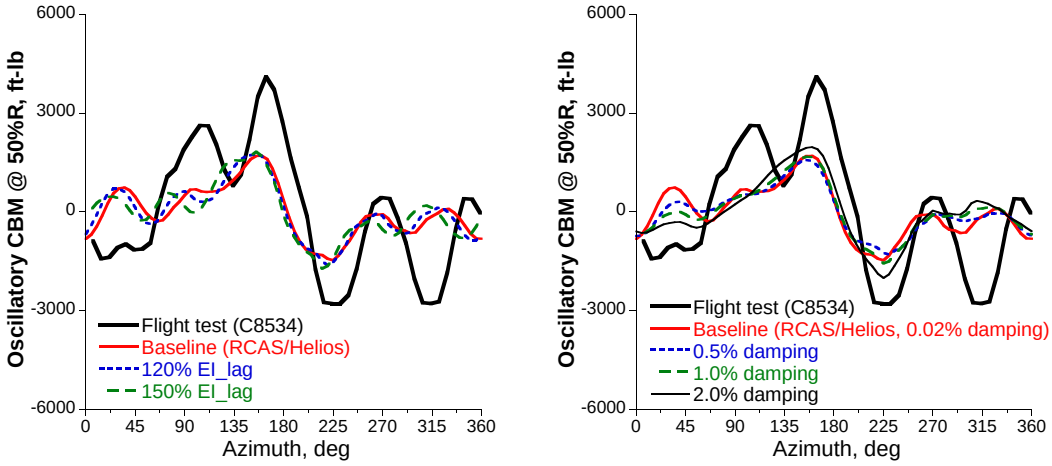

(a) Effect of chord stiffness (b) Effect of structural damping

Fig. 20. Effects of stiffness and damping variations on chord bending moments @ 50%R, μ = 0.37, C_T/σ = 0.081 (C8534).

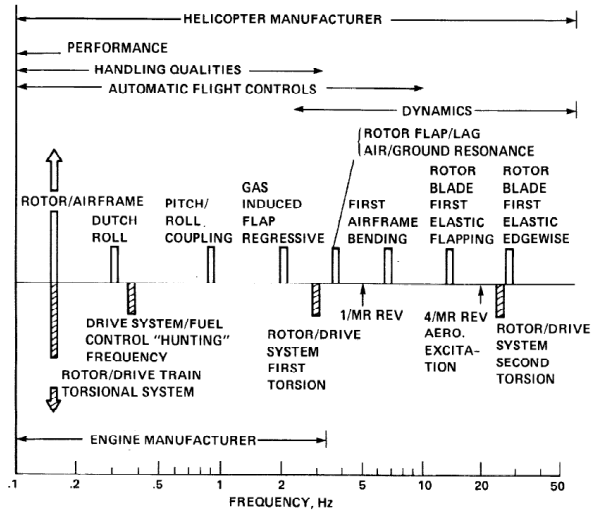

Fig. 21. Modal frequencies of rotorcraft dynamics system (Ref. 30).

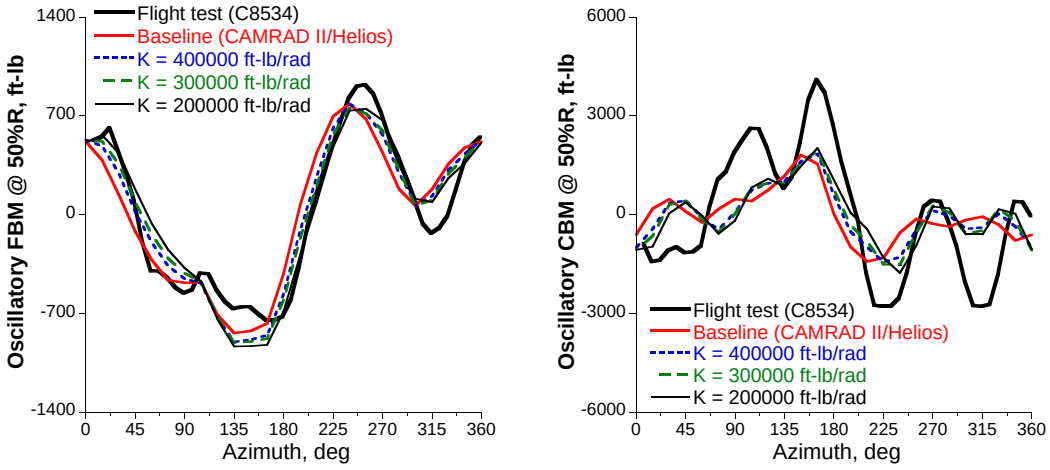

(a) Flap bending moment @ 50%R (b) Chord bending moment @ 50%R

Fig. 22. Effects of drivetrain stiffness on flap and chord bending moments, μ = 0.37, C_T/σ = 0.081 (C8534).

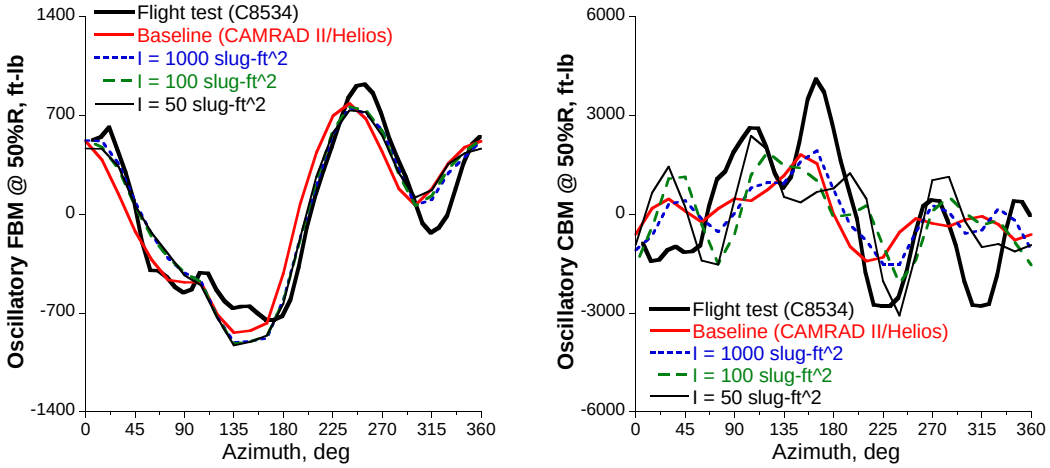

(a) Flap bending moment @ 50%R

(b) Chord bending moment @ 50%R

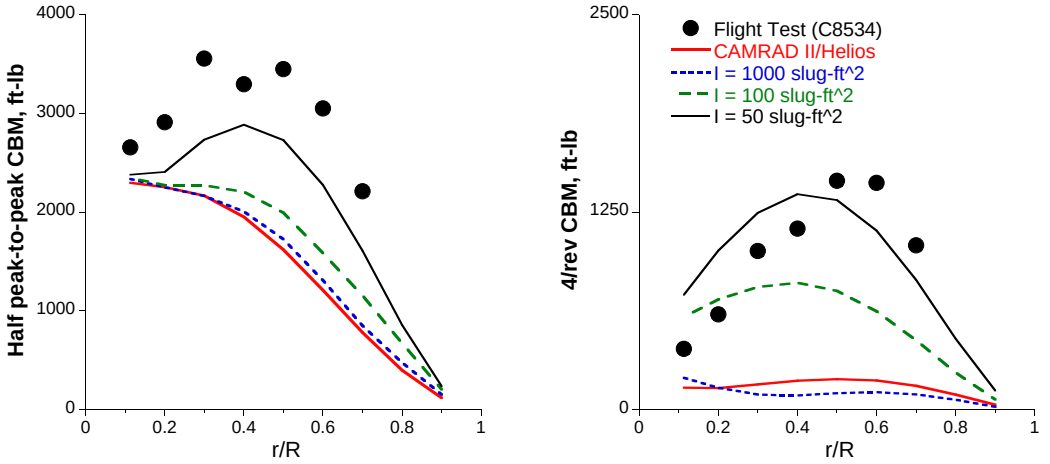

(c) Half peak-to-peak chord bending moment

(d) 4/rev chord bending moment

Fig. 23. Effects of drivetrain inertia on flap and chord bending moments, μ = 0.37, C_T/σ = 0.081 (C8534).